nature biomedical engineering

Article

https://doi.org/10.1038/s41551-022-00989-w

Intradermally delivered mRNA-encapsulating extracellular vesicles for collagen-replacement therapy

Received: 1 April 2022

Accepted: 18 November 2022

Published online: 12 January 2023

Check for updates

Yi You[1,2,13], Yu Tian[1,2,13], Zhaogang Yang[3,4,13], Junfeng Shi[5], Kwang Joo Kwak[5], Yuhao Tong[1,2], Andreanne Poppy Estania[1,2], Jianhong Cao[1,2], Wei-Hsiang Hsu[1,2], Yutong Liu[1,2], Chi-Ling Chiang[6], Benjamin R. Schrank[3], Kristin Huntoon[7,12], DaeYong Lee[7,12], Ziwei Li[4], Yarong Zhao[4], Huan Zhang[4], Thomas D. Gallup[7,12], JongHoon Ha[3], Shiyan Dong[3], Xuefeng Li[3,8], Yifan Wang[3], Wen-Jing Lu[9,10], Eman Bahrani[11], Ly James Lee[5], Lesheng Teng[4], Wen Jiang[3], Feng Lan[9] ✉, Betty Y. S. Kim[7,12] ✉ & Andrew S. Lee[1,2] ✉

The success of messenger RNA therapeutics largely depends on the availability of delivery systems that enable the safe, effective and stable translation of genetic material into functional proteins. Here we show that extracellular vesicles (EVs) produced via cellular nanoporation from human dermal fibroblasts, and encapsulating mRNA encoding for extracellular-matrix α1 type-I collagen (COL1A1) induced the formation of collagen-protein grafts and reduced wrinkle formation in the collagen-depleted dermal tissue of mice with photoaged skin. We also show that the intradermal delivery of the mRNA-loaded EVs via a microneedle array led to the prolonged and more uniform synthesis and replacement of collagen in the dermis of the animals. The intradermal delivery of EV-based COL1A1 mRNA may make for an effective protein-replacement therapy for the treatment of photoaged skin.

Recent developments in messenger RNA-modification techniques have enhanced the therapeutic efficiency of mRNA delivery and its potential for near-term clinical applications, including protein-replacement therapy and vaccination against the severe acute respiratory syndrome coronavirus 2 (SARS-CoV-2) virus[1,2]. However, the intrinsic inability and potential immunogenicity of mRNAs require that they be encapsulated within delivery vehicles. Current mRNA-delivery modalities centre on the usage of lipid nanoparticle (LNP) carriers for encapsulation and

[1]Peking University Shenzhen Graduate School, Shenzhen, China. [2]Institute of Cancer Research, Shenzhen Bay Laboratory, Shenzhen, China. [3]Department of Radiation Oncology, The University of Texas MD Anderson Cancer Center, Houston, TX, USA. [4]School of Life Sciences, Jilin University, Changchun, China. [5]Spot Biosystems Ltd., Palo Alto, CA, USA. [6]Department of Chemical and Biomolecular Engineering, The Ohio State University, Columbus, OH, USA. [7]Department of Neurosurgery, The University of Texas MD Anderson Cancer Center, Houston, TX, USA. [8]The Sixth Affiliated Hospital of Guangzhou Medical University, Qingyuan People's Hospital; State Key Laboratory of Respiratory Disease, Sino-French Hoffmann Institute, School of Basic Medical Sciences, Guangzhou Medical University, Guangzhou, China. [9]Fuwai Hospital Chinese Academy of Medical Sciences Shenzhen, Shenzhen Key Laboratory of Cardiovascular Disease, State Key Laboratory of Cardiovascular Disease and Peking Union Medical College, Shenzhen, China. [10]Beijing Laboratory for Cardiovascular Precision Medicine, The Key Laboratory of Biomedical Engineering for Cardiovascular Disease Research, The Key Laboratory of Remodeling-Related Cardiovascular Disease, Ministry of Education, Beijing Anzhen Hospital, Capital Medical University, Beijing, China. [11]Department of Dermatology, Vanderbilt University Medical Center, Nashville, TN, USA. [12]Brain Tumor Center, The University of Texas MD Anderson Cancer Center, Houston, USA. [13]These authors contributed equally: Yi You, Yu Tian and Zhaogang Yang. ✉e-mail: Fenglan@fuwai.com; bykim@mdanderson.org; Alee@pku.edu.cn

transport[3,4]. However, LNPs pose several major challenges, including cytotoxicity, poor biodistribution, lack of target specificity and immunogenicity. These problems may be caused by the requirement for the surface PEGylation (PEG stands for poly(ethylene glycol)) of LNPs to improve their circulatory half-life and to reduce non-specific clearance[5,6]. Notably, the administration of LNPs in people has been linked to anaphylaxis, hypersensitivity and autoimmune adverse events[7,8]. Therefore, the identification of mRNA carriers that can overcome some of these LNP-associated challenges would be helpful for the further development of mRNA-based therapeutics.

Extracellular vesicles (EVs), including exosomes and microvesicles, play a major role in the transport of biomolecules and nucleic acids, including mRNAs, within the human body[9–11]. As a result, in recent years, EVs have emerged as promising carriers for nucleic-acid-based therapeutics owing to their intrinsic biocompatibility, their ability to cross physiological barriers and their low immunogenicity[12,13]. Unlike LNPs, EVs, including exosomes, are endogenously produced by the body's cells and lead to lower levels of inflammatory responses. Moreover, strategies to cheaply and easily produce large quantities of exosomes have been developed. We previously reported a cellular nanoporation (CNP) method in which transient nanometric pores were created on the surface of source cells to allow for the large-scale loading of full-transcript mRNAs into secreted EVs[14]. Here, by using a mouse model of acute photoaging that closely mimics the pathophysiological features of aging-damaged skin in humans[15], we show the utility of exosome-based *COL1A1* mRNA therapy to replace dermal collagen-protein loss as an anti-aging treatment for photoaged skin. To improve the efficiency of mRNA delivery and retention, we also show that the delivery of collagen mRNA via a hyaluronic acid (HA) microneedle (*COL1A1*-EV MN) patch allows for a more efficient distribution of mRNA in the dermis, resulting in durable collagen-protein engraftment and in an improved treatment of wrinkles in photoaged skin.

Results

Preparation and in vitro delivery of *COL1A1* mRNA-containing EVs

Dermal atrophy owing to irreversible loss of collagen is a hallmark of skin aging[16,17]. Numerous methods have aimed to restore loss of collagen protein in skin, ranging from over the counter and pharmaceutical approaches (antioxidants[18–20], retinoids[21], peptides[22,23]) to medical devices (that is, laser therapy[24] and synthetic dermal fillers[25,26]). However, none of these existing technologies have been able to achieve long-term endogenous collagen replacement to maintain skin strength, firmness and elasticity over time[27–29]. Stimulating fibroblasts responsible for synthesizing collagen proteins can also be an effective way for short-term control of skin aging[30]. However, fibroblasts gradually lose their capacity to proliferate and synthesize collagen as they senesce, resulting in challenges for longer-term methods of collagen replacement for anti-aging treatment[31]. To overcome these limitations, we aimed to replace collagen protein in a photoaging collagen-depletion model via EV-mediated mRNA delivery. To generate EVs loaded with human collagen I alpha I (*COL1A1*) mRNA, we employed a CNP technique that involved plating a monolayer of neonatal human dermal fibroblasts (nHDFs) on a nanopore surface and nano-transfecting the cells with a *COL1A1-GFP* plasmid (Fig. 1a and Supplementary Fig. 1a)[14]. EVs were isolated from culture media the day after transfection. CNP-treated cells were found to have a 10-fold higher EV number per cell as compared with cells treated with standard bulk electroporation (BEP), which was performed using cuvette-style parallel electrodes as previously described[32], or untreated nHDFs in culture (Fig. 1b). The EVs produced by each method were characterized by a size distribution peaking at about 150 nm in diameter as determined by nanoparticle tracking analysis (NTA) and 80% of intensity in the mode peak by dynamic light scattering (DLS) (Fig. 1c and Supplementary Fig. 1b,c) with a polydispersity index (PDI) of 0.12–0.25. Western blot experiments showed that expressions of exosome (CD9, CD63, TSG101) and microvesicle (ARF6) biomarkers in the CNP-treated group were significantly higher than in the untreated group, confirming the increase in secreted EVs (Supplementary Fig. 1d). Kinetic analyses further showed that voltage-optimized EV release peaked at 8 h after CNP induction, with continued secretion noted over the next 24 h (Supplementary Fig. 1e,f). Reverse transcription-quantitative polymerase chain reaction (RT–qPCR) showed that CNP-secreted EVs contained more than 200 times the *COL1A*1 mRNA than BEP-secreted EVs and 3,000-fold higher *COL1A1* mRNA than EVs secreted from non-transfected cells (Fig. 1d). Bioanalyser assessment of gel agarose demonstrated full-length transcribed *COL1A1* mRNA at ~4,000 nucleotides (Fig. 1e). EVs prepared by CNP exhibited structural stability when stored for preclinical administration at 4 °C with no changes in appearance, membrane and size properties when evaluated by cryo-electron microscopy (cryo-EM), atomic force microscopy (AFM) and NTA (Supplementary Fig. 2a–c). Furthermore, *COL1A1* mRNA encapsulated within EVs was stable both at room temperature and at 4 °C, and also exhibited serum stability, thereby highlighting their potential for future clinical utility (Supplementary Fig. 2d,e).

To assess the therapeutic potential of *COL1A1* mRNA-containing EVs (*COL1A1*-EVs) in vitro, we treated cultured fibroblasts with *COL1A1*-EVs for 48 h (Supplementary Fig. 3a). Proliferation of fibroblasts was observed to increase with *COL1A1*-EV treatment in a dose-dependent manner (Fig. 1f). After treatment, elevated COL1A1 protein expression was observed in fibroblasts treated with *COL1A1*-EVs, as evidenced by increased co-localization of green fluorescent protein (GFP) with COL1A1 under immunofluorescence microscopy. In contrast, COL1A1 levels were substantially lower without co-localization of GFP in the non-treated group (Extended Data Fig. 1a,b). Successful mRNA delivery into recipient cells was further confirmed by elevated collagen mRNA expression and collagen protein levels measured via quantitative PCR and western blot analysis, respectively, in fibroblasts treated with *COL1A1*-EVs (Extended Data Fig. 1c,d and Supplementary Fig. 3b). Moreover, pro-collagen I, a precursor of COL1 protein, was significantly increased following *COL1A1*-EV treatment, indicating improved COL1 protein synthesis by the EV-treated fibroblasts compared with untreated fibroblasts (Extended Data Fig. 1e). Confocal microscopy imaging of cellular uptake of EVs indicated that EV cargo delivery into recipient cells is mediated by clathrin-mediated endocytosis (Supplementary Fig. 3c,d) and is capable of lysosome escape (Supplementary Fig. 4). Taken together, these findings demonstrate that functional *COL1A1* mRNA can be stably encapsulated within EVs by CNP and that this *COL1A1*-EV delivery system can significantly increase COL1A1 protein expression in vitro.

In vivo kinetics of *COL1A1* mRNA expression and protein translation following *COL1A1*-EV delivery

To understand the kinetics of EV-mediated *COL1A1* mRNA delivery and protein formation in vivo, we delivered 2.7×10^9 copy number of *COL1A1* mRNA *COL1A1*-EVs into the dermis of mice via an insulin needle syringe. The mice were killed over the next 14 d for histological analysis by RNAscope for *COL1A1* mRNA quantification. *COL1A1* mRNA was found to be significantly elevated in local skin tissue at 12 h after delivery, with notable decreases observed at 24 h and 48 h after injection, and a return to baseline *COL1A1* mRNA levels by 96 h (Fig. 2a,b). In vivo translation of *COL1A1* mRNA into protein was assessed by immunofluorescence microscopy of explanted tissue over a 30 d period. GFP+ COL1A1+ immunostained grafts were observed as early as 12 h after injection, with peak fluorescence at 4 d after delivery (Fig. 2c–e). GFP+ COL1A1+ protein grafts were observed to decrease in a time-dependent manner from day 4 to day 30 after injection as observed by immunofluorescence microscopy, with the majority of *COL1A1*-EV-derived protein turning over by day 30. These findings demonstrate that lower doses of *COL1A1*-EV delivery results in a 3–4 d

https://doi.org/10.1038/s41551-022-00989-w

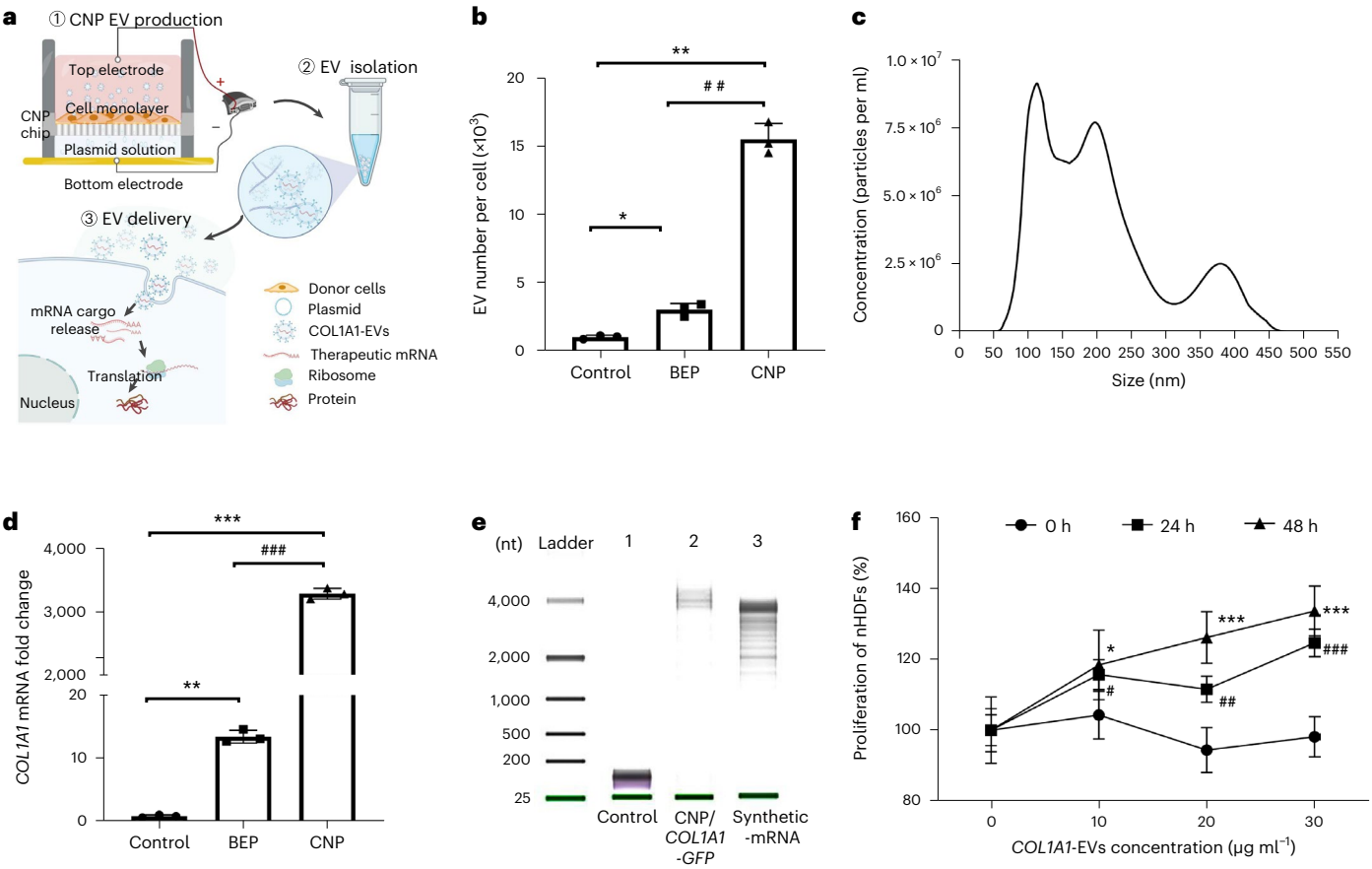

Fig. 1 | CNP generates large quantities of EVs loaded with *COL1A1* mRNA. **a**, Schematic representation of CNP-generated EVs for targeted nucleic acid delivery. **b**, EV number per cell produced by untreated nHDFs in PBS buffer as control, BEP or CNP with PBS buffer only in 24 h ($n = 3$ for each group; $^{*}P = 0.048$ Control vs BEP; $^{**}P = 0.005$ Control vs CNP; $^{\#\#}P = 0.002$ BEP vs CNP). **c**, Characterization of EVs by nanoparticle tracking analysis. **d**, RT–qPCR of *COL1A1* mRNA reveals that EVs produced by CNP contain much larger quantities of transcribed mRNAs than EVs produced by BEP and Control groups in 24 h ($n = 3$ for all groups; $^{**}P = 0.002$ Control vs BEP; $^{***}P < 0.001$ Control vs CNP; $^{\#\#\#}P < 0.001$ BEP vs CNP). **e**, Gel electrophoresis of total RNA extracted from 3.78×10^8 EVs produced from CNP using *COL1A1-GFP* plasmid compared with synthetic in vitro-transcribed *COL1A1* mRNA as control. **f**, Proliferation of nHDFs after treatment with different protein concentrations of *COL1A1*-EVs at 0 h, 24 h and 48 h ($n = 4$ for all groups; at 24 h: $^{\#}P = 0.0107$, 10 μg ml^{-1} vs 0 μg ml^{-1} of protein concentration of *COL1A1*-EVs after treatment; $^{\#\#}P = 0.002$, 20 μg ml^{-1} vs 0 μg ml^{-1}; $^{\#\#\#}P < 0.001$, 30 μg ml^{-1} vs 0 μg ml^{-1}; at 48 h: $^{*}P = 0.045$, 10 μg ml^{-1} vs 0 μg ml^{-1} of *COL1A1*-EV treatment; $^{***}P < 0.001$, 20 μg ml^{-1} vs 0 μg ml^{-1}; $^{***}P < 0.001$, 30 μg ml^{-1} vs 0 μg ml^{-1}). All data are from three independent experiments and are presented as means ± s.e.m. Two-sided Student's *t*-tests were used for the comparisons in **b** and **d**. One-way ANOVA was used for the comparisons in **f**. The schematic in **a** was created with BioRender.com.

peak of COL1A1 protein in recipient tissues, decreasing to baseline levels by day 30 after injection.

In vivo therapeutic efficacy of *COL1A1*-EVs in a collagen-depletion skin-photoaging model

Dermal photoaging is characterized by the destruction of collagen and extracellular-matrix (ECM) proteins in the skin by sun exposure and UV irradiation, which causes the formation of wrinkles[33,34]. To assess the capacity of *COL1A1* mRNA EVs to replace degraded collagen protein in vivo, we employed a previously described photoaging model in which athymic nude mice were treated with UV (311 nm) irradiation over an 8 week period, resulting in dermal wrinkles secondary to collagen depletion[35] (Supplementary Fig. 5a). The efficacy of the 8 week UV irradiation course in degrading collagen and elastin fibres in murine skin was confirmed by histological and tissue analysis (Supplementary Fig. 5b–g). We next assessed the therapeutic potential of *COL1A1*-EVs to replace dermal collagen in UV-irradiated mice by treating the animals with a 5x injection course of either: (1) 2.7×10^9 copy number of *COL1A1* mRNA encapsulated in EVs (*COL1A1*-EVs), (2) 2.7×10^9 copy number of *COL1A1* mRNA encapsulated in lipid nanoparticles (*COL1A1*-LNPs), (3) control EVs without CNP cargo loading (unloaded EVs), (4) 0.05% retinoic acid topical treatment (RA) or (5) saline control. Wrinkle formation was tracked at days 0, 4, 7, 14, 21 and 28 after initiation of treatment, and all animals were killed at day 28 for histology and skin plaster replica analyses[36] (Fig. 3a). Microscopic photography of dermal skin wrinkles over the treatment period demonstrated modest decreases in wrinkle number and area by day 28 for the *COL1A1*-LNPs, unloaded EVs and retinoic acid groups compared with the saline control group (Fig. 3b). In contrast, photoaged mice treated with *COL1A1*-EVs exhibited a reduction in wrinkle number and area beginning on day 7 after treatment initiation, with a significant reduction from day 14 onward to levels similar to those observed in unirradiated sham controls (Fig. 3c,d). Skin plaster replicas of the dorsal skin taken at day 28 after treatment initiation confirmed the effectiveness of *COL1A1*-EVs for treating photoaged skin as compared with saline control, retinoic acid, unloaded EV controls and *COL1A1*-LNPs (Extended Data Fig. 2). Noticeably, *COL1A1*-LNPs also exhibited a reduction in wrinkle number and area compared with saline control, retinoic acid and unloaded EV controls, although this effect was not as pronounced as with *COL1A1*-EVs. Skin treated with *COL1A1*-EVs and *COL1A1*-LNPs also demonstrated higher elasticity and

https://doi.org/10.1038/s41551-022-00989-w

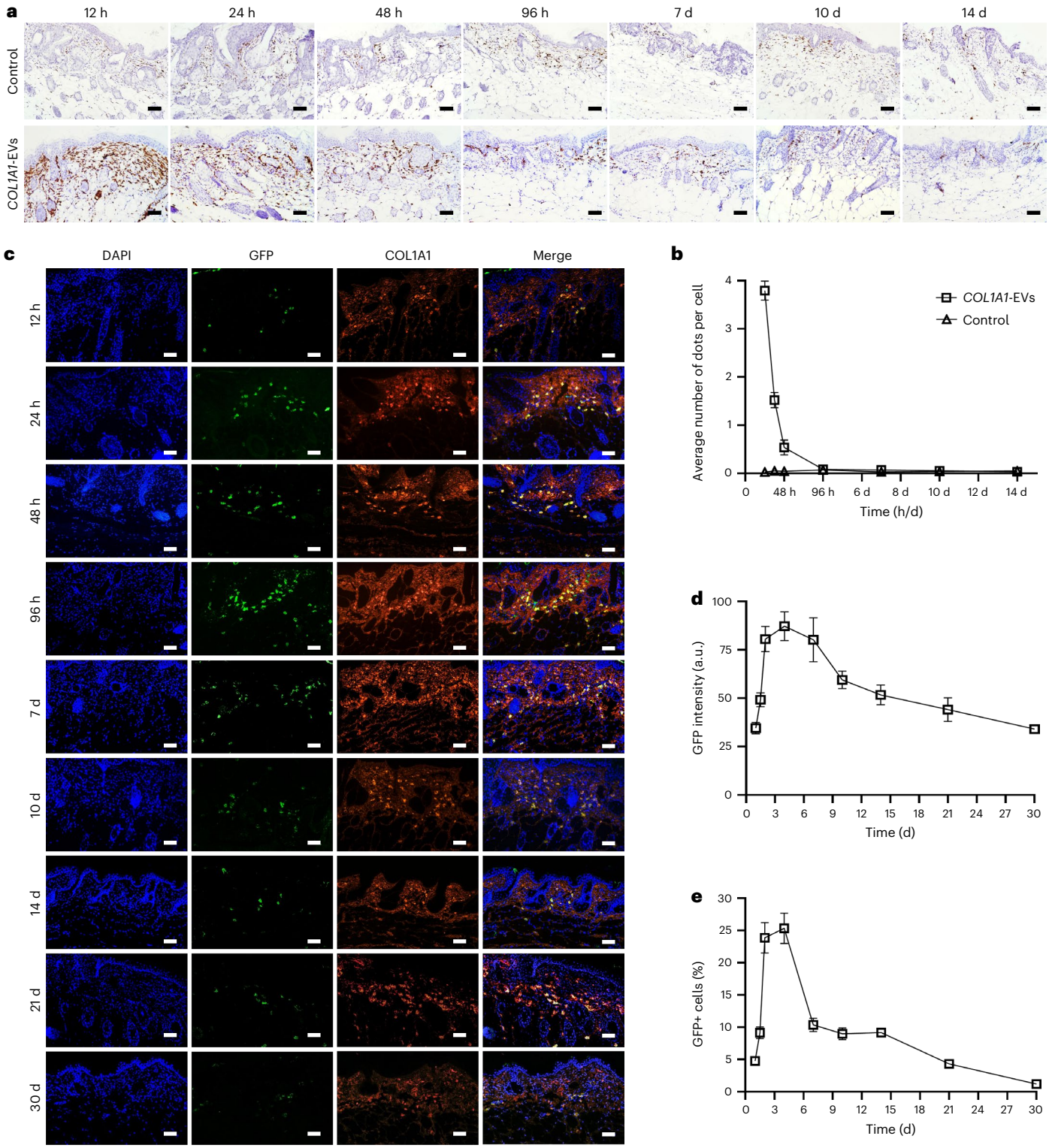

Fig. 2 | In vivo kinetics of *COL1A1*-EV mRNA delivery and protein formation in murine skin. a, In situ hybridization of human *COL1A1* mRNA by RNAscope after intradermal injection of *COL1A1*-EVs and saline control, measured at 12 h, 24 h, 48 h, 96 h, 7 d, 10 d and 14 d after injection. Scale bar,100 µm. **b**, Quantification of RNAscope results by average number of brown dots per cell. **c**, Immunofluorescence over time of *COL1A1*-EV-derived protein by visualization of co-localized GFP and COL1A1 protein (RFP). Scale bar, 100 µm. **d**, Fluorescence intensity quantification of COL1A1-GFP protein expression. **e**, Quantification of GFP+ cells confirms that the *COL1A1*-EV-derived protein grafts decrease in a time-dependent manner over 30 d. All data are from three independent experiments and are presented as means ± s.e.m.

firmness as measured by a cutometer and an Instron extensometer, respectively (Supplementary Fig. 6).

To assess the immunogenic side effects of *COL1A1*-LNPs and *COL1A1*-EVs, treated skin was excised from a subgroup of animals and analysed for inflammation 24 h after injection. Skin treated with *COL1A1*-LNPs exhibited redness and swelling as compared with sham controls and skin treated with *COL1A1*-EVs (Extended Data Fig. 3a). Flow cytometry and enzyme-linked immunoassay (ELISA) of tissue further

https://doi.org/10.1038/s41551-022-00989-w

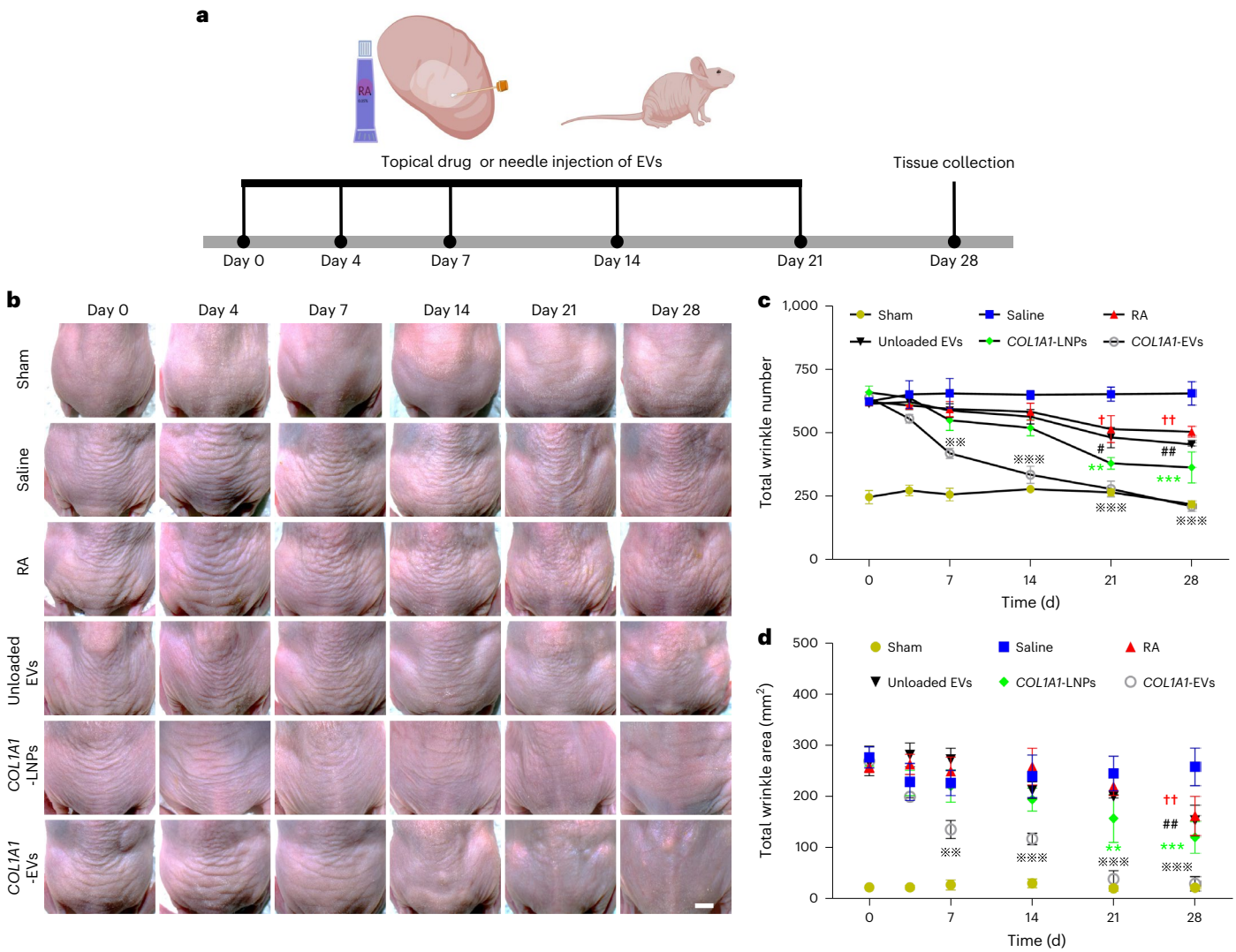

Fig. 3 | *COL1A1*-EV mRNA delivery reduces dermal wrinkles in a UV-irradiation photoaging model. a, Schematic representation and timeline of 5 low-dose injections of *COL1A1*-EVs (2.7×10^9 copy number *COL1A1* mRNA per dose). Skin tissue was collected at 28 d. **b**, Wrinkle formation was tracked at days 0, 4, 7, 14, 21 and 28 after initial delivery of *COL1A1*-EVs, *COL1A1*-LNPs, unloaded EVs, 0.05% retinoic acid (RA) or saline ($n = 4$ for all groups). The sham group comprised female nude mice that were not exposed to UV irradiation. Scale bar, 5 mm. **c**, Total numbers of dorsal-skin wrinkles quantified with custom software ($n = 4$ for all groups; $^{※※}P = 0.0016$ *COL1A1*-EVs vs Saline at day 7; $^{※※※}P < 0.001$ *COL1A1*-EVs vs Saline at days 14, 21 and 28; $^{**}P = 0.0089$ *COL1A1*-LNPs vs Saline at day 21; $^{**}P = 0.0097$ *COL1A1*-LNPs vs Saline at day 28; $^{\#}P = 0.461$ Unloaded EVs vs Saline at day 21; $^{\#\#}P = 0.0034$ Unloaded EVs vs Saline at day 28; $^{\dagger}P = 0.0142$ RA vs Saline at day 21; $^{\dagger\dagger}P = 0.0069$ RA vs Saline at day 28). **d**, Quantification of wrinkle area on dorsal skin ($n = 4$ for all groups; $^{※※}P = 0.0063$ *COL1A1*-EVs vs Saline at day 7; $^{※※※}P < 0.001$ *COL1A1*-EVs vs Saline at days 14, 21 and 28; $^{**}P = 0.0082$ *COL1A1*-LNPs vs Saline at day 21; $^{***}P < 0.001$ *COL1A1*-LNPs vs Saline at day 28; $^{\dagger\dagger}P = 0.0040$ RA vs Saline at day 28; $^{\#\#}P = 0.0018$ Unloaded EVs vs Saline at day 28). All data are from three independent experiments and are presented as means ± s.e.m. Two-way ANOVA was used for the comparisons in **c** and **d**. The schematic in **a** was created with BioRender.com.

revealed massive leucocytic infiltrate dominated by neutrophils in tissue that received *COL1A1*-LNPs (Extended Data Fig. 3b,c) and high levels of inflammatory cytokines such as TNF-α, IL-6, IL-1β and IFN-γ (Extended Data Fig. 3d–f). By comparison, tissue that received *COL1A1*-EV treatment did not exhibit a strong inflammatory reaction. These findings suggest that LNPs are substantially more immunogenic than EVs.

After assessment at day 28, a subset of animals was retained for 4 additional weeks to monitor wrinkle reduction duration. Dermal wrinkles were seen to reappear as early as 1 week later, beginning at day 35 after treatment initiation, and by day 56, dermal wrinkles were statistically indistinguishable from pre-treatment levels (Extended Data Fig. 4).

To evaluate dermal collagen engraftment from *COL1A*1-EV delivery, skin was excised from all groups at day 28 after treatment initiation and evaluated by immunofluorescence microscopy, as well as Masson trichrome staining. Histological analysis and fluorescence intensity quantification revealed that COL1A1 protein expression was significantly restored after *COL1A1*-EV treatment relative to other groups (Fig. 4a,b). Masson trichrome staining confirmed higher levels of collagen staining and dermal thickness (197.95 ± 24.46 μm *COL1A1*-EVs vs 95.19 ± 10.66 μm Saline at day 28, $P < 0.001$) in mice given *COL1A1*-EVs than in mice given saline control, retinoic acid, unloaded EVs or *COL1A1*-LNPs (Fig. 4c,d).

Design of a microneedle-based system for the delivery of EV mRNAs

As wrinkles were found to return to baseline levels in photoaged animals within 1 month of *COLA1*-EV treatment cessation, we next aimed to improve the duration of protein replacement and the effectiveness of collagen engraftment by designing an HA microneedle formulation

https://doi.org/10.1038/s41551-022-00989-w

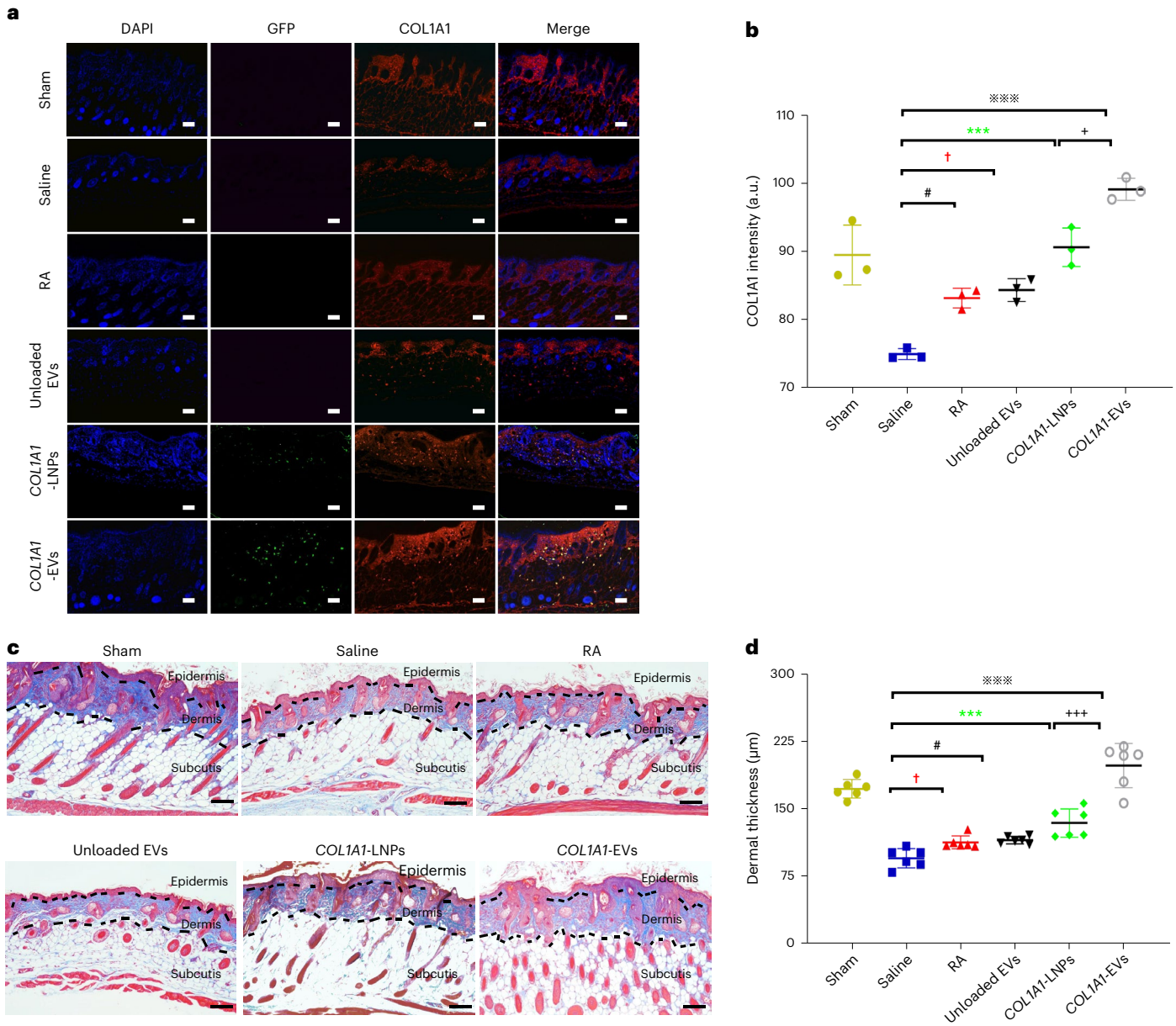

Fig. 4 | Histologic analysis demonstrates collagen replacement in the dermis of photoaged mice treated with *COL1A1*-EV mRNA. a, Immunofluorescence staining for GFP and COL1A1 (RFP) protein in sham control group, saline control group, RA treatment group, unloaded EV treatment group, *COL1A1*-LNPs and *COL1A1*-EV treatment groups. *COL1A1*-EV-treated mice exhibited GFP+ COL1A1 protein grafts in the dermis and subcutis at 28 d after initiation of treatment. Scale bar, 200 μm. **b**, Fluorescence intensity of COL1A1 protein (RFP) for all treatment groups ($n = 3$ for all groups; $^{***}P < 0.001$ *COL1A1*-EVs vs Saline; $^{***}P < 0.001$ *COL1A1*-LNPs vs Saline; $^{\#}P = 0.0386$ Unloaded EVs vs Saline; $^{\dagger}P = 0.0218$ RA vs Saline; $^{+}P = 0.0255$ *COL1A1*-EVs vs *COL1A1*-LNPs). **c**, Representative Masson trichrome collagen staining of the epidermis, dermis and subcutis for all mouse groups. Collagen is blue. Scale bar, 200 μm. **d**, Quantification of dermal thickness showing increased collagen fibres in the *COL1A1*-EVs group ($n = 3$ for all groups; $^{***}P < 0.001$ *COL1A1*-EVs vs Saline; $^{***}P < 0.001$ *COL1A1*-LNPs vs Saline; $^{\#}P = 0.0437$ Unloaded EVs vs Saline; $^{\dagger}P = 0.0447$ RA vs Saline; $^{+++}P < 0.001$ *COL1A1*-EVs vs *COL1A1*-LNPs). All data are from three independent experiments and are presented as means ± s.e.m. One-way ANOVA was used for the comparisons in **b** and **d**.

(*COL1A1*-EV MN) to improve EV-mediated mRNA tissue delivery. Custom microneedle patches were prepared by using a micromoulding method in which *COL1A1*-EVs were mixed with a 15% HA solution dissolved in PBS and cast into the tips of a polydimethylsiloxane (PDMS) mould by maintaining a vacuum for 30 min, after which 1 ml of 15 wt% HA solution was placed into the micromould and then transferred to 4 °C for 4 h for solidification (Fig. 5a). Each needle of the *COL1A1*-EV microneedle patch was moulded in a conical shape, with a circular diameter of 400 μm at their base and a height of 1,000 μm (Fig. 5b). The mechanical strength of patches with 10%, 15% or 20% HA loaded with EVs was evaluated with a tensile testing machine (Supplementary Fig. 7a). The load fracture force of our 15% *COL1A1*-EV MN was confirmed to be higher than the minimum average force needed for skin penetration (0.058 N)[37] (Supplementary Fig. 7b). Haematoxylin and eosin (H&E) staining confirmed that the microneedles penetrated through the stratum corneum into the dermis (516 ± 76 μm)[38] (Fig. 5c). *COL1A1*-EVs loaded into HA microneedles were found to have stable appearance and membrane integrity as evaluated by transmission electron microscopy (TEM) and AFM, as well as stable *COL1A1* mRNA and particle size distribution (Supplementary Fig. 7c–f). For delivery into tissue, *COL1A1*-EV MN patches were pressed into the dorsal skin of mice, and the microneedle base was removed after 15 min (Supplementary Video 1). During this period, the microneedles

https://doi.org/10.1038/s41551-022-00989-w

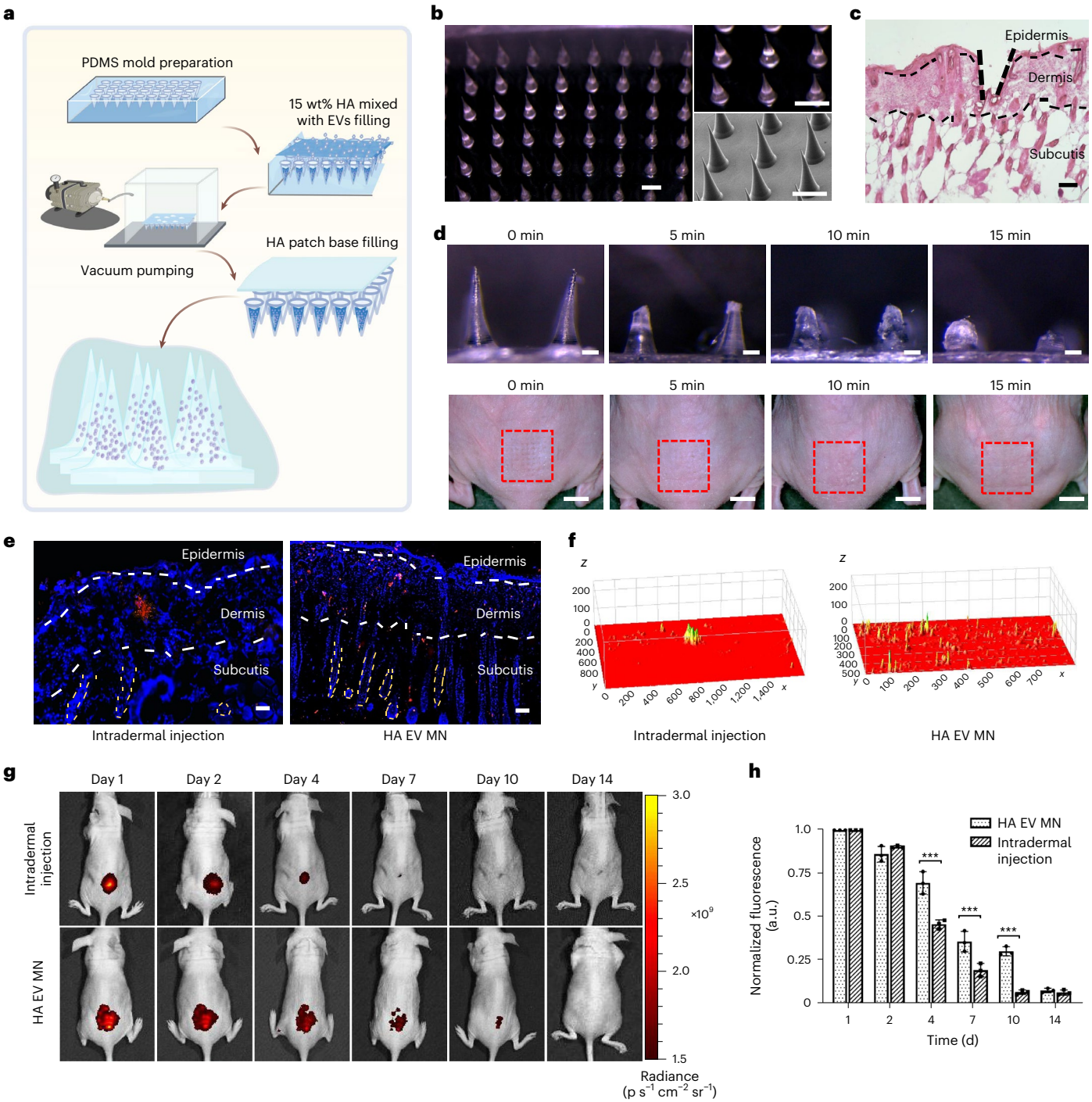

Fig. 5 | A microneedle delivery system for improved EV distribution in tissue. **a**, Schematic illustration of microneedle fabrication. **b**, Microscope and scanning electron microscopy images of microneedle arrays. Scale bar, 500 µm. **c**, H&E-stained section of mouse skin shows penetration of single microneedle. Scale bar, 100 µm. **d**, Top: time course of HA EV microneedle tips pressed into skin; the microneedles dissolved within 15 min of application. Scale bars, 200 µm. Bottom: skin recovery after HA EV microneedle treatment shows minimal irritation. Scale bars, 5 mm. **e**, Skin histology of Dil-labelled EVs shows highly concentrated EVs (red) unevenly distributed in the subcutis after syringe needle injection, whereas microneedle-delivered EVs were more evenly distributed in tissue. Yellow dashed lines encircle representative subcutaneous hair bulbs and border representative rod-like portions of the follicle extending upward to the dermis. Scale bar, 100 µm. **f**, Representative EV distribution analysed by ImageJ software. **g**, In vivo fluorescence images of nude mice treated with intradermal injection or HA microneedle patch delivery of Dil-labelled EVs on days 1, 2, 4, 7, 10 and 14 after delivery ($n = 3$ for all groups). **h**, Quantification of fluorescence intensity over the 14 d treatment period. Data are normalized to the fluorescence intensity at day 1. All data are from three independent experiments and are presented as means ± s.e.m. ***$P < 0.001$ *COL1A1*-EV MN delivery group vs needle delivery group. Two-way ANOVA was used for the comparisons in **h**. The schematic in **a** was created with BioRender.com.

dissolved completely, with no visible skin irritation or marking at the site of administration (Fig. 5d and Supplementary Video 2). To compare the tissue distribution of EVs delivered via microneedle with that of EVs delivered by insulin syringe, EVs were labelled with DiI (1,1′-dioctadecyl-3,3,3′,3′-tetramethylindocarbocyanine perchlorate; Beyotime, C1036)[39] and administered intradermally under the dorsal

https://doi.org/10.1038/s41551-022-00989-w

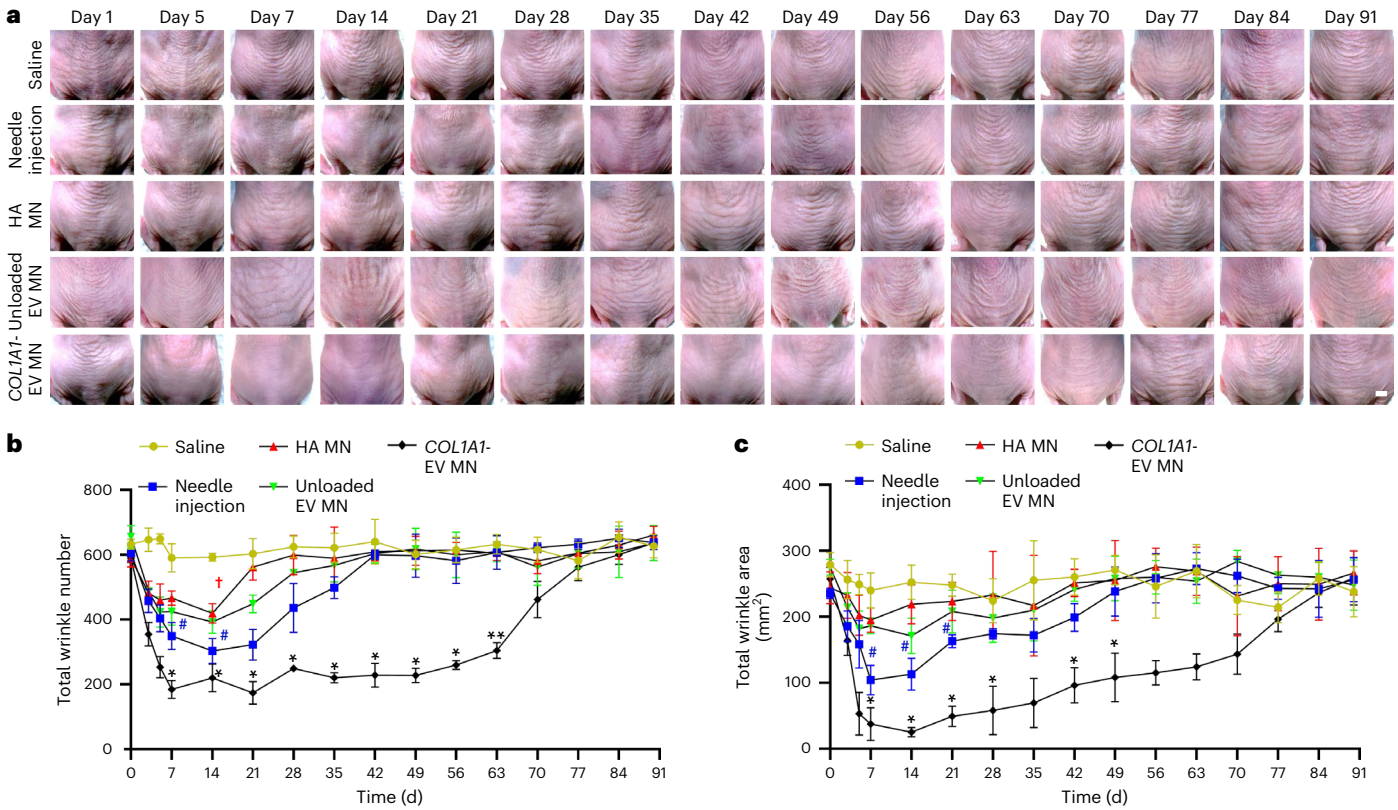

Fig. 6 | *COL1A1*-EV delivery via *COL1A1*-EV microneedle improves long-term treatment of photoaged skin. a, Long-term (91 d) observation of 4 treatment groups after a single injection: (1) saline control, (2) *COL1A1*-EVs (22×10^9 copy number *COL1A1* mRNA) delivered by 28G syringe needle, (3) HA microneedle control, (4) unloaded EVs delivered by HA microneedle (Unloaded EV microneedle) and (5) *COL1A1*-EV MN (22×10^9 copy number *COL1A1* mRNA), ($n = 4$ for all groups). Scale bar, 5 mm **b**, Quantification of total numbers of wrinkles ($n = 4$ for all groups; $^*P = 0.014$ *COL1A1*-EV MN vs Saline at day 7; $^*P = 0.038$ *COL1A1*-EV MN vs Saline at day 14; $^*P = 0.012$ *COL1A1*-EV MN vs Saline at day 21; $^*P = 0.039$ COL1A1-EV MN vs Saline at day 28; $^*P = 0.031$ *COL1A1*-EV MN vs Saline at day 35; $^*P = 0.03$ *COL1A1*-EV MN vs Saline at day 42; $^*P = 0.022$ *COL1A1*-EV MN vs Saline at day 49; $^*P = 0.031$ *COL1A1*-EV MN vs Saline at day 56; $^{**}P = 0.008$ *COL1A1*-EV MN vs Saline at day 63; $^{\#}P = 0.030$ Needle injection vs Saline at day 7; $^{\#}P = 0.041$ Needle injection vs Saline at day 14; $^{\dagger}P = 0.047$ HA microneedle vs Saline at day 14). **c**, Quantification of total dorsal skin wrinkle area ($n = 4$ for all groups; $^*P = 0.016$ *COL1A1*-EV MN vs Saline at day 7; $^*P = 0.038$ *COL1A1*-EV MN vs Saline at day 14; $^*P = 0.042$ *COL1A1*-EV MN vs Saline at days 21 and 28; $^*P = 0.026$ *COL1A1*-EV MN vs Saline at day 42; $^*P = 0.048$ *COL1A1*-EV MN vs Saline at day 49; $^{\#}P = 0.033$ Needle injection vs Saline at day 7; $^{\#}P = 0.031$ Needle injection vs Saline at day 14; $^{\#}P = 0.042$ Needle injection vs Saline at day 21). All data are from three independent experiments and are presented as means ± s.e.m. Two-way ANOVA was used for the comparisons in **b** and **c**.

skin of recipient mice, with subsequent histological assessment by immunofluorescence microscopy (Fig. 5e and Supplementary Fig. 8a,b). Tissue distribution analysis revealed that syringe needle injection resulted in uneven delivery of EVs with clumping in specific areas of the dermis and subcutis, whereas EVs delivered by microneedle were better dispersed in the dermis and subcutis (Fig. 5f and Supplementary Fig. 8c,d). Assessment of EV membrane integrity by cryo-EM showed less EV membrane lysis in the EVs delivered with the microneedle patch vs the syringe needle (18.1 ± 3.0% *COL1A1*-EV MN vs 28.3 ± 2.4% needle injection, $P = 0.022$) (Supplementary Fig. 8e,f). To assess whether the improved tissue distribution and EV membrane protection resulted in improved EV engraftment, we next employed serial in vivo fluorescence imaging of DiI-labelled EVs injected intradermally in mice over a 14 d period. Fluorescence imaging confirmed similar DiI EV signal between syringe-delivered EVs and microneedle-delivered EVs for the first 4 d after injection. However, the *COL1A1*-EV microneedle group had significantly higher fluorescence signal at day 4 (69.61 ± 6.4% *COL1A1*-EV MN vs 45.79 ± 2.5% needle injection, $P < 0.001$) and at day 7 (35.78 ± 5.9% *COL1A1*-EV MN vs 19.38 ± 3.8% needle injection, $P < 0.001$), lasting up to day 10 post injection (30.22 ± 2.6% *COL1A1*-EV MN vs 6.68 ± 1.3% needle injection, $P < 0.001$) (Fig. 5g,h). Ex vivo organ distribution analyses of DiI probe fluorescence over a 2 week time period revealed similar tissue distribution and signal decay across animals receiving intradermal injection and animals receiving microneedle delivery, suggesting that the reduction in signal intensity is due to metabolism of the DiI probe as shown in other similar studies[40,41] (Supplementary Fig. 9a,b). Taken together, these findings indicate that use of the microneedle patch improves long-term retainment of EVs in tissue.

Therapeutic efficacy of *COL1A1*-EV delivery via microneedles

We next tested whether use of our custom *COL1A1*-EV microneedle patch for delivering *COL1A1*-EVs could result in improved in vivo protein replacement in the skin of photoaged mice (Supplementary Fig. 10). Athymic mice were again subjected to 8 weeks UV irradiation and assigned to 1 of 5 treatment groups: (1) saline control, (2) *COL1A1* mRNA EVs delivered by syringe needle, (3) HA microneedle control, (4) unloaded EVs delivered by HA microneedle (Unloaded EV microneedle) and (5) *COL1A1* mRNA-loaded EVs delivered by HA microneedle (*COL1A1*-EV MN). All mice were given a single-dose injection of 22×10^9 copy number of *COL1A1* mRNA (or an equivalent vehicle volume for control groups) at day 0 of the treatment timeline. After injection, all mice were monitored via microscopic photography of dorsal skin wrinkles for up to 3 months (Fig. 6a). Relative to syringe needle injection, which reduced wrinkle formation for up to 35 d before a return to pre-treatment baseline, delivery of *COL1A1* mRNA by *COL1A1*-EV MN was found to substantially reduce wrinkle area and number for

up to 70 d before a return to baseline levels (Fig. 6b,c). To further confirm these findings, a subset of mice from each group were killed at 1 month, 2 months and 3 months after treatment for skin replica plaster assessment of the dorsal skin and histology (Extended Data Fig. 5a–c). Both needle injection and *COL1A1*-EV MN treatments reduced wrinkle length and depth for up to 1 month post treatment (Extended Data Fig. 5d,e). However, only mice treated with *COL1A1*-EV MN showed significantly long-lasting reductions in wrinkle length and depth for up to the 2 month timepoint. To test whether collagen replacement and wrinkle treatment could be maintained for a longer period of time, we subjected additional animal cohorts to serial treatment of *COL1A1*-EVs delivered by syringe needle and microneedle every 30 d. Both *COL1A1*-EVs delivered by syringe needle and *COL1A1*-EV MN were found to reduce wrinkle number and area for as long as the animals received treatment, with *COL1A1*-EV MN animals demonstrating the most improvement (Extended Data Fig. 6).

Histologic analysis of skin samples taken after treatment confirmed the lasting engraftment of GFP+ COL1A1 protein engraftment in the dermis and subcutis of mice in both the needle injection group and the *COL1A1*-EV microneedle group at 1 month after delivery (Fig. 7a). However, by the 2 month timepoint, only the mice in the *COL1A1*-EV microneedle cohort demonstrated GFP+ COL1A1 engraftment in the dermis and subcutis (Fig. 7b). At 3 months after delivery, skin samples in all groups failed to exhibit any GFP collagen engraftment (Fig. 7c). COL1A1+ GFP immunofluorescence intensity was quantified, supporting wrinkle microscopy findings which demonstrated effective treatment at days 30–60 and a return to pre-treatment baseline from days 70–90 (Fig. 7d). Immunohistochemical staining of COL1A1 protein and Masson trichrome staining of skin tissues confirmed that the amount of collagen in the dermis correlated with immunofluorescence microscopy findings and that among all cohorts, the *COL1A1*-EV MN group had the most abundant collagen fibres and highest dermal thickness (180.14 ± 21.46 µm *COL1A1*-EV MN vs 96.61 ± 14.00 µm Saline at 1 month, $P < 0.001$; 154.88 ± 8.27 µm *COL1A1*-EV MN vs 109.25 ± 10.86 µm Saline at 2 months, $P < 0.05$) (Fig. 7e,f). Taken together, these findings indicate that encapsulation and delivery of *COL1A1* mRNA via our *COL1A1*-EV MN system can prolong collagen protein replacement in photoaged skin for more than twice the duration of syringe needle delivery.

Discussion

Extracellular vesicles have emerged as a next-generation drug-delivery system because of their inherent properties of biocompatibility, low immunogenicity and ability to be derived from healthy human cells[12]. Nonetheless, most studies focusing on nucleic-acid delivery so far have encapsulated small molecules in the 10–20 nt range such as microRNAs and small interfering RNA (siRNAs) as the payload, whereas larger nucleic acids such as mRNAs are seldom evaluated owing to the difficulty of loading them into EVs[42]. With the recent advancement in utility of mRNA-based therapeutics for treating human diseases, there has been increased interest in using EVs as an mRNA-delivery system. Recently, we developed an mRNA-loading technique that allows for the large-scale production of EVs containing intact endogenous mRNA for nucleic-acid therapy[14]. Here we have shown that mRNA-loaded EVs can be applied for protein-replacement therapy in a model of dermal collagen photodepletion[17]. We have shown that CNP is able to load high copy numbers of *COL1A1* mRNA (~4,000+ nt) into EVs, which cannot be achieved by post-insertion loading methods[43,44]. In vivo results showed that these *COL1A1*-EVs can restore COL1A1 protein expression in the mouse skin after photoaging. We also examined the presence of *COL1A1* mRNA and protein over time in vivo, and found that the corresponding protein was translated as early as 12 h after delivery with a peak at 4 d, and that this was sustained for several weeks, depending on dose. Several studies have generated ex vivo COL1A1 protein as a collagen filler; here we characterized the in vivo kinetics of exogenous *COL1A1* mRNA delivery and protein expression in vivo[45].

To adapt our approach for long-term protein replacement, we further developed a microneedle array for the delivery of *COL1A1*-EVs to allow for an even distribution of EVs into local tissue, with reduced membrane rupture. HA is a critical element of the extracellular matrix and has been verified to have excellent biocompatibility with skin tissues and various biomaterial systems[46,47]. By integrating EVs into an HA microneedle biomaterial, we were able to extend protein engraftment of COL1A1 to more than 60 d in the skin specimens evaluated. Notably, EVs not loaded with *COL1A1* mRNA were also able to achieve a modest decrease in wrinkle number, which is consistent with studies finding that 'empty' EVs from certain parental cells are potential therapeutic candidates owing to endogenous cargos (still, the detailed mechanisms underlying such phenomena need further exploration)[36].

Compared with the relatively long-lasting expression of DNA-based gene therapies, mRNA therapeutics may help advance gene therapy and lower the risks of adverse events owing to the retention of the mRNAs in the cytoplasm, without penetration into the nucleus[48,49]. Hence, mRNA-based modalities have advantages over DNA-based and virus-based gene therapies, such as the ability to bypass the traditional transcription process, and no risk of genomic integration (as opposed to the use of some adeno-associated virus vectors, which traditionally has been considered to have a low risk profile[50]). However, the clinical translation of mRNA therapeutics is still limited. For mRNA products developed using LNPs, the immunogenicity of PEGylation components on the LNP surface as well as some carrier formulations have been linked to inflammation and to numerous adverse safety events[51,52]. Indeed, when we compared the delivery of *COL1A1*-LNPs and *COL1A1*-EVs in vivo, we found that *COL1A1*-LNPs were able to yield collagen protein and reduce dermal wrinkles, but also caused notable inflammatory infiltrate in local tissue, whereas *COL1A1*-EVs did not. Several recent studies have shown that EVs are characterized by low levels of immunogenicity, with some preclinical reports and clinical trials (clinicaltrials.gov: NCT05191381, NCT05216562) suggesting that EVs derived from a variety of cell types have immunosuppressive effects, although it should be noted that these studies primarily used mesenchymal stromal cells and dendritic cells as donor cell types[36,53,54].

Future challenges for the clinical application of *COL1A1*-EV MN include the optimization of microneedle geometry with more densely protected EVs as well as optimized storage conditions because mRNA is subject to rapid degradation when not retained at −80 °C or below[55]. Ideally, future EV systems can be packaged as ready-to-use aliquots and shipped at appropriate temperatures, which would greatly improve the practicability of *COL1A1*-EV MN systems for clinical use. We would

Fig. 7 | *COL1A1*-EV mRNA delivery via *COL1A1*-EV MN results in long-term protein replacement in skin. a–c Immunofluorescence staining of GFP and COL1A1 (RFP) demonstrates GFP-positive COL1A1 protein grafts in the skin of mice receiving *COL1A1*-EVs via 28G needle injection and via *COL1A1*-EV MN for up to 1 month (28 d) after delivery. At 2 months (63 d), only mice that were treated with *COL1A1*-EV MN had long-term GFP-positive COL1A1 engraftment. No evidence of GFP-positive collagen protein could be detected in any mice by 3 months (91 d) after delivery. Scale bar, 200 µm. **d**, Quantification of GFP and COL1A1 (RFP) co-localized fluorescence signal demonstrates long-term *COL1A1*-EV-derived collagen engraftment in the skin of mice given *COL1A1*-EV MN vs mice given *COL1A1*-EVs via 28G needle injection and control groups ($n = 3$ for all groups; $^{***}P < 0.001$ *COL1A1*-EV MN vs Needle injection at 2 months). **e**, Immunohistochemical staining of COL1A1 protein and Masson trichrome staining at 1 month (28 d), 2 months (63 d) and 3 months (91 d). Scale bar, 200 µm. **f**, Quantification of dermal thickness by Masson trichrome staining ($n = 3$ for all groups; $^{**}P = 0.0062$ *COL1A1*-EV MN vs Saline at 1 month; $^{*}P = 0.034$ *COL1A1*-EV MN vs Saline at 2 months). All data are from three independent experiments and are presented as means ± s.e.m. Two-way ANOVA was used for the comparisons in **d** and **f**.

https://doi.org/10.1038/s41551-022-00989-w

also aim to expand therapeutic applications in our system to include items such as COL7 for genetic orphan diseases such as epidermolysis bullosa[56]. We have only delivered mRNA via the microneedle system, yet the system is also suitable for packaging other types of EV cargos, such as miRNAs and siRNAs, and other bioactive therapeutic agents such as peptides and proteins[57–59]. Although many challenges would need to be overcome before the microneedle-based EV-delivery system can be tried in humans, because of the improved biocompatibility and benign side-effect profile of EVs as compared with LNPs and adeno-associated virus (AAV), we believe that the system might constitute a universal

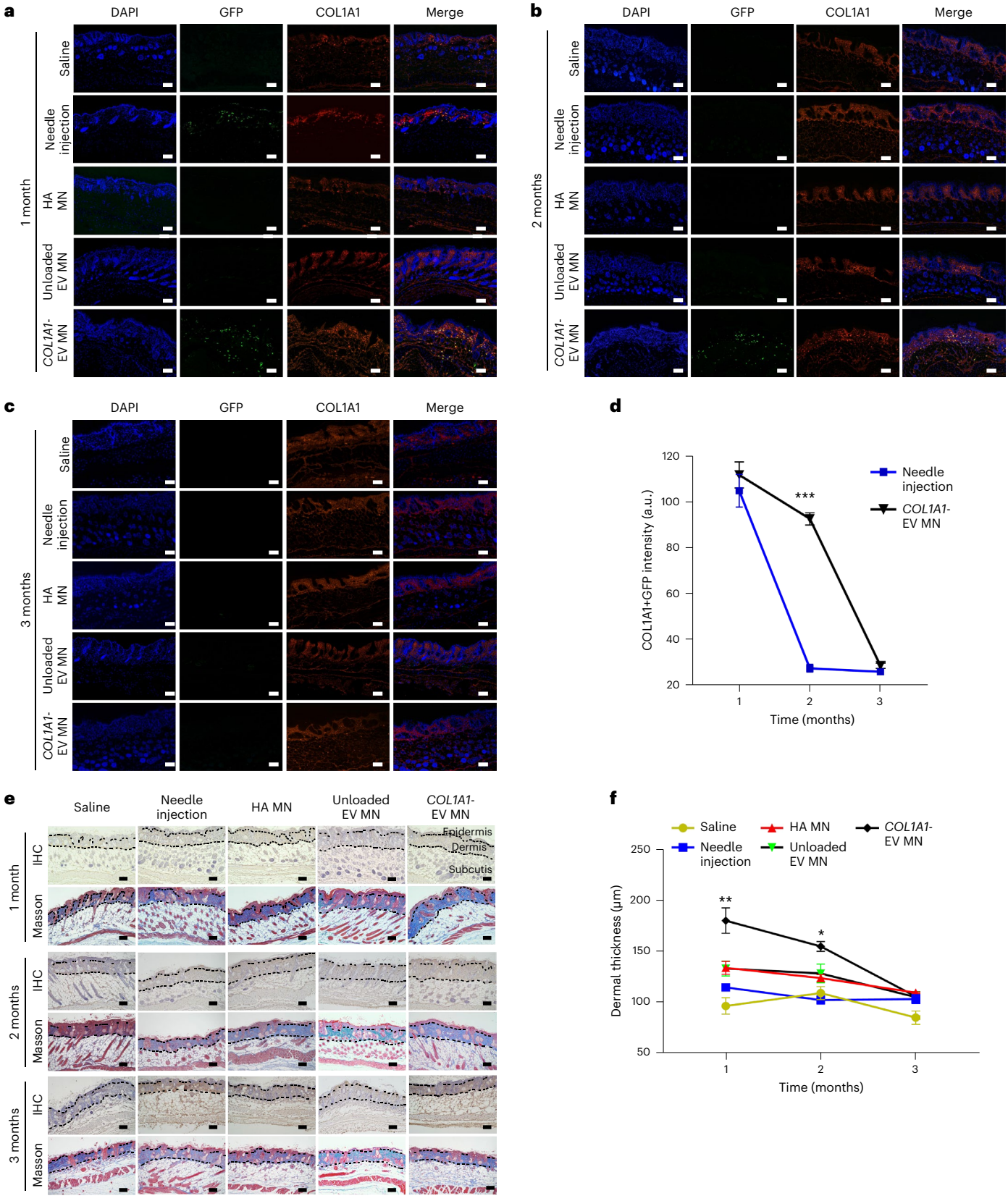

nucleic-acid carrier for the treatment of a range of human diseases and conditions.

Methods

Cell culture

nHDFs (PCS-201-010) were purchased from ATCC and cultured in DMEM medium (Thermo Fisher) containing 10% heat-inactivated fetal bovine serum (FBS; 10099141C, Thermo Fisher) at 37 °C in humidified conditions equilibrated with 5% CO_2.

Cellular nanoporation and electroporation

For CNP, a single layer of nHDF was seeded on a 1 cm × 1 cm 3D CNP surface for overnight incubation as previously described. Human *COL1A1 cDNA* (NM_000088.3) plasmid with GFP tag was purchased from Sino Biological (HG11776-ACG). Plasmids pre-loaded in PBS buffer were injected into individual cells via nanochannels using an electric field strength of 250 V cm^{-1} with 10 pulses at 10 ms per pulse, with a 0.1 s interval. Various electroporation conditions were tested to determine optimal conditions. BEP (gene pulser xcell, Bio-rad) was conducted using an electric field strength of 1,250 V cm^{-1} with 1 pulse of 20 ms. *pCMV-COL1A1-GFP* plasmids were prepared at a concentration of 500 ng ml^{-1} in PBS for transfection.

Collection and purification of EVs secreted by donor cells

Cells were cultured in DMEM medium containing serum. The cell culture medium containing serum was removed when conducting CNP. Cells were then washed with PBS 3 times and cultured in serum-free cell culture medium for 24 h after CNP. EVs were collected from cell culture supernatants. In brief, the cell culture medium (CCM) was centrifuged at 200 × *g* for 5 min to remove cells and debris, after which it was centrifuged again at 2,000 × *g* for 30 min. Amicon Ultra-4 centrifugal filter unit (10 kDa, Millipore, 801024) was used to concentrate the CCM. The EV sample was purified using total exosome isolation reagent (Invitrogen, 4478360). EV particle size and number were measured using NanoSight NS300 (Malvern). The RNA yield and size distribution were analysed using an Agilent 2100 Bioanalyzer with an RNA 6000 Pico kit (Agilent Technologies).

RT–qPCR of EV-containing RNA expression levels

The expression of human *COL1A1* mRNA in EVs was measured using RT–qPCR following the manufacturer's recommended protocol. In brief, total RNA from purified EVs was obtained using an RNA purification mini kit (Norgen Biotek, 55000) and a DNA removal kit (Norgen Biotek, 25720). A SuperScript III First-Strand Synthesis system (Invitrogen) was used to synthesize the first-strand complementary DNA, with random hexamers as primers. The expression of genes was measured using TB Green Premix Ex *Taq* II (Takara, RR820). The primer sequences used were as follows: *COL1A1* (human), forward: 5′-CCTGGAAAGAATGGAGATGA-3′ and reverse: 5′-ACCATCCAAACCACTGAAAC-3′; *Gapdh* (human), forward: 5′-CAGCCTCAAGATCATCAGCA - 3′ and reverse: 5′ - AGAGGCAGGGATGATGTTCT - 3′ (Supplementary Table 1).

In situ hybridization for human *COL1A1* mRNA in skin tissue

Nude female mice (10–12 weeks old) were anaesthetized with isoflurane, and the dorsal skin region was injected with 50 µl 2.7×10^9 copy number of CNP *COL1A1* mRNA EVs. At predefined timepoints (12, 24, 48, 96 h, 7 d, 10 d, 14 d) following the skin injection, the skin was excised and put in 4% formaldehyde for fixation. Subsequently, the slices were embedded in paraffin further sectioned into 4 µm slices. RNAscope automated in situ hybridization assay for detection of human *COL1A1* mRNA was performed using the HybEZ II Hybridization System (Advanced Cell Diagnostics (ACD)), and all in situ hybridization reagents were ACD products. In brief, target retrieval was performed at 95 °C for 15 min using Leica Epitope Retrieval Buffer 2, followed by protease treatment at 42 °C for 15 min. The probe (RNAscope Probe- Hs-COL1A1, 401891, ACD) was hybridized for 2 h at 40 °C followed by RNA scope amplification, and RNAscope 2.5 HD Assay BROWN kit was used for visualization of staining. RNAscope 2.5 LS probe-Rn-Ppib was used as negative control.

Immunofluorescence microscopy

Tissue sections were fixed with 4% paraformaldehyde for 20 min at room temperature and washed 3 times with PBS (Vetec) for 5 min each. Then the tissue was transferred to 0.2% Triton X-100 for 15 min (permeabilized), followed by blocking with BSA for 40 min and the addition of primary antibody (ab34710 and ab6556, Abcam) for overnight blocking at 4 °C. Finally, the secondary antibody (ab6939 and ab6717, Abcam) was added and the tissue sections placed at room temperature for 60 min. Tissue sections were then washed with PBS, added with DAPI (ThermoFisher) for nuclear staining and then mounted for observation.

Immunohistochemical staining and analysis

Tissue sections were fixed in 4% paraformaldehyde for 20 min, washed 3 times with PBS (pH 7.4) for 5 min each and then transferred to a retrieval box containing ethylenediaminetetraacetic acid (EDTA) (pH 9.0) antigen retrieval solution for antigen retrieval in a microwave oven. Subsequently, the sections were incubated in 3% hydrogen peroxide solution at room temperature for 25 min in the dark. After washing with PBS, the tissue was evenly covered with 3% BSA or 10% normal rabbit serum, blocked at room temperature for 30 min, added with primary antibody (ab34710 and ab6556, Abcam) and incubated overnight at 4 °C. Then, a secondary antibody (HRP-labelled) corresponding to the primary antibody was added to cover the tissue sections, which were then incubated at room temperature for 50 min. For 3,3'-diaminobenzidine (DAB) colour development, the slides were placed in PBS (pH 7.4) and washed 3 times with shaking on a de-staining shaker for 5 min each time. After the slices were slightly dried, the freshly prepared DAB colour developing solution was added dropwise in the circle. Developing time was controlled under the microscope. Haematoxylin, haematoxylin differentiation solution and hematoxylin blue-returning solution were sequentially added for nuclei counterstaining. Finally, the glass slides were placed in anhydrous ethanol and xylene for dehydration and sealing.

Mice

Animal work was approved by the Institutional Animal Care and Use Committee (IACUC) of Shenzhen Bay Laboratory (No. D2021-107) or partner laboratories. To create the skin-photoaging model, female nude mice (10–12 weeks old) were subjected to UVB irradiation of the dorsal skin every other day for 8 weeks as follows: mice were anaesthetized with 1.5% isoflurane, and then UV irradiation was delivered with a UV lamp (Philips; emission spectrum 311 nm) positioned 30 cm above the dorsal skin of the mice every other day for 8 weeks. The UV irradiation intensity, represented as the minimal erythemal dose (MED), was set at 1 MED during the first 2 weeks (60 mJ cm^{-2}), elevated to 2 MED (120 mJ cm^{-2}) in the third week, 3 MED (180 mJ cm^{-2}) in the fourth week and 4 MED (240 mJ cm^{-2}) during the fifth to eighth weeks of the experiment. The total irradiated UVB volume was approximately 80 MED. For the syringe-based treatment of photoaged skin, nude mice, after the 8 week irradiation period described above, were assigned to 1 of 6 treatment groups (4 mice each): (1) UVB irradiation + saline, (2) UVB irradiation + 0.05% retinoic acid, (3) UVB irradiation + unloaded nHDF-EVs delivered with a 32G Hamilton syringe, (4) UVB irradiation + 2.7×10^9 copy number *COL1A1* mRNA *COL1A1*-LNPs, (5) UVB irradiation + 2.7×10^9 copy number *COL1A1* mRNA *COL1A1*-EVs delivered with a 32G Hamilton syringe and (6) no UVB exposure (sham). Skin treatments took place on days 0, 4, 7, 14 and 21. The whole back skin was divided into three parts for analysis.

Skin replica

A SILFLO silicone replica and ring locator were purchased from Clinical & Derm. Replicas of the back (dorsal) skin of the mice were obtained

at the end of the treatment period. The replicas were analysed by stereomicroscopy (Olympus SZX7), and corresponding images were analysed by ImageJ (NIH).

Preparation of *COL1A1*-EV MN patches and local tissue delivery

The fabrication of the microneedle patch was performed using a silicone micromould, with each needle cavity being 400 µm in a round base diameter and 1,000 µm in height. These needle cavities were arranged in a 10 × 10 array with 700 µm tip to tip spacing. For the preparation of the microneedle patch, 150 µl of 15 wt% HA solution was mixed with 50 µl EVs, kept under vacuum for 30 min and then transferred to 4 °C until it was deposited in the needle cavity. Finally, 1 ml of 15 wt% HA solution was loaded onto the micromould and the micromould placed in a drying chest with an attached fan to accelerate the evaporation process for solidification. After solidification, the microneedle patch was detached from the silicone mould for further use. To assess *COL1A1*-EV delivery via the customized microneedle patches, nude mice were irradiated for 8 weeks as described above and assigned to 1 of 5 treatment groups (4 mice each): (1) UVB irradiation + saline, (2) UVB irradiation + 22×10^9 copy number *COL1A1* mRNA *COL1A1*-EVs delivered by 28G Hamilton syringe, (3) UVB irradiation + HA microneedle patch, (4) UVB irradiation + 10^{10} unloaded nHDF-EVs delivered via microneedle (unloaded EV microneedle) and (5) UVB irradiation + 15% HA microneedle mixed with 22×10^9 copy number *COL1A1* mRNA *COL1A1*- EVs.

Fluorescence in vivo imaging

Microneedle-treated mice were imaged with an in vivo imaging system (IVIS Spectrum, Perkin Elmer) on days 1, 2, 4, 7, 10 and 14. The parameters were set as follows: exposure time 15 s, excitation 570 nm, emission 680 nm, 2F/stop and 13.6 cm field of view in the specified fluorescence imaging times. Quantitative analysis of RFP fluorescence intensity was performed by measuring the average radiation efficiency (photon s^{-1} cm^{-2} sr^{-1} μW^{-1}) in a region of interest. Data were normalized to fluorescence intensity on day 1.

Statistical analysis

Quantitative data are represented as mean ± s.e.m. No data were excluded in this study. To analyse the statistical difference between two groups, two-sided Student's *t*-tests were used for the comparisons. For two or more groups, one-way analysis of variance (ANOVA) with Tukey's multiple-comparison test was used to analyse the statistical difference. Two-way ANOVA was chosen for analysing the statistical difference between data points in groups. $P < 0.05$ was considered statistically significant. GraphPad Prism 8.3 was used for data analysis.

Reporting summary

Further information on research design is available in the Nature Portfolio Reporting Summary linked to this article.

Data availability

The main data supporting the results in this study are available within the paper and its Supplementary Information. Source data for the figures are available from figshare at https://figshare.com/articles/dataset/SD_FIGS_xlsx/21514641. The raw and analysed datasets generated during the study are available for research purposes from the corresponding authors on reasonable request.

References

1. Sahin, U., Kariko, K. & Tureci, O. mRNA-based therapeutics–developing a new class of drugs. *Nat. Rev. Drug Discov.* **13**, 759–780 (2014).
2. Muik, A. et al. Neutralization of SARS-CoV-2 Omicron by BNT162b2 mRNA vaccine-elicited human sera. *Science* **375**, 678–680 (2022).
3. Kowalski, P. S., Rudra, A., Miao, L. & Anderson, D. G. Delivering the messenger: advances in technologies for therapeutic mRNA delivery. *Mol. Ther.* **27**, 710–728 (2019).
4. Wang, C., Zhang, Y. & Dong, Y. Lipid nanoparticle-mRNA formulations for therapeutic applications. *Acc. Chem. Res.* **54**, 4283–4293 (2021).
5. Qiu, M., Li, Y., Bloomer, H. & Xu, Q. Developing biodegradable lipid nanoparticles for intracellular mRNA delivery and genome editing. *Acc. Chem. Res.* **54**, 4001–4011 (2021).
6. Lokugamage, M. P. et al. Mild innate immune activation overrides efficient nanoparticle-mediated RNA delivery. *Adv. Mater.* **32**, e1904905 (2020).
7. Szebeni, J. et al. Applying lessons learned from nanomedicines to understand rare hypersensitivity reactions to mRNA-based SARS-CoV-2 vaccines. *Nat. Nanotechnol.* **17**, 337–346 (2022).
8. Moghimi, S. M. Allergic reactions and anaphylaxis to LNP-based COVID-19 vaccines. *Mol. Ther.* **29**, 898–900 (2021).
9. Valadi, H. et al. Exosome-mediated transfer of mRNAs and microRNAs is a novel mechanism of genetic exchange between cells. *Nat. Cell Biol.* **9**, 654–659 (2007).
10. Cheng, L. & Hill, A. F. Therapeutically harnessing extracellular vesicles. *Nat. Rev. Drug Discov.* **21**, 379–399 (2022).
11. de Jong, O. G. et al. Drug delivery with extracellular vesicles: from imagination to innovation. *Acc. Chem. Res.* **52**, 1761–1770 (2019).
12. Herrmann, I. K., Wood, M. J. A. & Fuhrmann, G. Extracellular vesicles as a next-generation drug delivery platform. *Nat. Nanotechnol.* **16**, 748–759 (2021).
13. van Niel, G., D'Angelo, G. & Raposo, G. Shedding light on the cell biology of extracellular vesicles. *Nat. Rev. Mol. Cell Biol.* **19**, 213–228 (2018).
14. Yang, Z. et al. Large-scale generation of functional mRNA-encapsulating exosomes via cellular nanoporation. *Nat. Biomed. Eng.* **4**, 69–83 (2020).
15. Sharma, M. R., Werth, B. & Werth, V. P. Animal models of acute photodamage: comparisons of anatomic, cellular and molecular responses in C57BL/6J, SKH1 and Balb/c mice. *Photochem. Photobiol.* **87**, 690–698 (2011).
16. Varani, J. et al. Decreased collagen production in chronologically aged skin: roles of age-dependent alteration in fibroblast function and defective mechanical stimulation. *Am. J. Pathol.* **168**, 1861–1868 (2006).
17. Fisher, G. J. W. Z. Pathophysiology of premature skin aging induced by ultraviolet light. *N. Engl. J. Med.* **337**, 1419–1428 (1997).
18. Buranasudja, V., Rani, D., Malla, A., Kobtrakul, K. & Vimolmangkang, S. Insights into antioxidant activities and anti-skin-aging potential of callus extract from *Centella asiatica* (L.). *Sci. Rep.* **11**, 13459 (2021).
19. Wada, N., Sakamoto, T. & Matsugo, S. Mycosporine-like amino acids and their derivatives as natural antioxidants. *Antioxidants* **4**, 603–646 (2015).
20. Xiong, Z. M. et al. Ultraviolet radiation protection potentials of methylene blue for human skin and coral reef health. *Sci. Rep.* **11**, 10871 (2021).
21. Bielli, A. et al. Cellular retinoic acid binding protein-II expression and its potential role in skin aging. *Aging* **11**, 1619–1632 (2019).
22. Song, H., Zhang, S., Zhang, L. & Li, B. Effect of orally administered collagen peptides from bovine bone on skin aging in chronologically aged mice. *Nutrients* **9**, 1209 (2017).
23. Jeong, S. et al. Anti-wrinkle benefits of peptides complex stimulating skin basement membrane proteins expression. *Int. J. Mol. Sci.* **21**, 73 (2019).
24. Lee, A. Y. Skin pigmentation abnormalities and their possible relationship with skin aging. *Int. J. Mol. Sci.* **22**, 3727 (2021).

25. Kim, J. H. et al. Comparative evaluation of the effectiveness of novel hyaluronic acid-polynucleotide complex dermal filler. *Sci. Rep.* **10**, 5127 (2020).
26. Urdiales-Galvez, F., Martin-Sanchez, S., Maiz-Jimenez, M., Castellano-Miralla, A. & Lionetti-Leone, L. Concomitant use of hyaluronic acid and laser in facial rejuvenation. *Aesthetic Plast. Surg.* **43**, 1061–1070 (2019).
27. Fisher, G. J., Varani, J. & Voorhees, J. J. Looking older: fibroblast collapse and therapeutic implications. *Arch. Dermatol.* **144**, 666–672 (2008).
28. Quan, T. et al. Enhancing structural support of the dermal microenvironment activates fibroblasts, endothelial cells, and keratinocytes in aged human skin in vivo. *J. Invest. Dermatol.* **133**, 658–667 (2013).
29. Shakouri, R. et al. In vivo study of the effects of a portable cold plasma device and vitamin C for skin rejuvenation. *Sci. Rep.* **11**, 21915 (2021).
30. de Araujo, R., Lobo, M., Trindade, K., Silva, D. F. & Pereira, N. Fibroblast growth factors: a controlling mechanism of skin aging. *Skin Pharmacol. Physiol.* **32**, 275–282 (2019).
31. Cole, M. A., Quan, T., Voorhees, J. J. & Fisher, G. J. Extracellular matrix regulation of fibroblast function: redefining our perspective on skin aging. *J. Cell Commun. Signal.* **12**, 35–43 (2018).
32. Shi, J. et al. A review on electroporation-based intracellular delivery. *Molecules* **23**, 3044 (2018).
33. Todorova, K. & Mandinova, A. Novel approaches for managing aged skin and nonmelanoma skin cancer. *Adv. Drug Deliv. Rev.* **153**, 18–27 (2020).
34. Choi, J. S. et al. Functional recovery in photo-damaged human dermal fibroblasts by human adipose-derived stem cell extracellular vesicles. *J. Extracell. Vesicles* **8**, 1565885 (2019).
35. Alpermann, H. & Vogel, H. G. Effect of repeated ultraviolet irradiation on skin of hairless mice. *Arch. Dermatol. Res.* **262**, 15–25 (1978).
36. Hu, S. et al. Needle-free injection of exosomes derived from human dermal fibroblast spheroids ameliorates skin photoaging. *ACS Nano* **13**, 11273–11282 (2019).
37. Kim, J. D., Kim, M., Yang, H., Lee, K. & Jung, H. Droplet-born air blowing: novel dissolving microneedle fabrication. *J. Control. Release* **170**, 430–436 (2013).
38. Abd, E. et al. Skin models for the testing of transdermal drugs. *Clin. Pharmacol.* **8**, 163–176 (2016).
39. Zheng, T. et al. Plasma exosomes spread and cluster around β-amyloid plaques in an animal model of Alzheimer's disease. *Front. Aging Neurosci.* **9**, 12 (2017).
40. Li, Z. et al. Exosome-based Ldlr gene therapy for familial hypercholesterolemia in a mouse model. *Theranostics* **11**, 2953–2965 (2021).
41. Cao, H. et al. In vivo real-time imaging of extracellular vesicles in liver regeneration via aggregation-induced emission luminogens. *ACS Nano* **13**, 3522–3533 (2019).
42. Kamerkar, S. et al. Exosomes facilitate therapeutic targeting of oncogenic KRAS in pancreatic cancer. *Nature* **546**, 498–503 (2017).
43. O'Brien, K., Breyne, K., Ughetto, S., Laurent, L. C. & Breakefield, X. O. RNA delivery by extracellular vesicles in mammalian cells and its applications. *Nat. Rev. Mol. Cell Biol.* **21**, 585–606 (2020).
44. Yin, H. et al. Non-viral vectors for gene-based therapy. *Nat. Rev. Genet.* **15**, 541–555 (2014).
45. Zhang, Z. et al. COL1A1: a potential therapeutic target for colorectal cancer expressing wild-type or mutant KRAS. *Int. J. Oncol.* **53**, 1869–1880 (2018).
46. Yu, J. et al. Microneedle-array patches loaded with hypoxia-sensitive vesicles provide fast glucose-responsive insulin delivery. *Proc. Natl Acad. Sci. USA* **112**, 8260–8265 (2015).
47. Wu, T. et al. Microneedle-mediated biomimetic cyclodextrin metal organic frameworks for active targeting and treatment of hypertrophic scars. *ACS Nano* **15**, 20087–20104 (2021).
48. Paunovska, K., Loughrey, D. & Dahlman, J. E. Drug delivery systems for RNA therapeutics. *Nat. Rev. Genet.* **23**, 265–280 (2022).
49. van Haasteren, J., Li, J., Scheideler, O. J., Murthy, N. & Schaffer, D. V. The delivery challenge: fulfilling the promise of therapeutic genome editing. *Nat. Biotechnol.* **38**, 845–855 (2020).
50. Mullard, A. Gene therapy community grapples with toxicity issues, as pipeline matures. *Nat. Rev. Drug Discov.* **20**, 804–805 (2021).
51. Shi, D. et al. To PEGylate or not to PEGylate: immunological properties of nanomedicine's most popular component, polyethylene glycol and its alternatives. *Adv. Drug Deliv. Rev.* **180**, 114079 (2022).
52. Knop, K., Hoogenboom, R., Fischer, D. & Schubert, U. S. Poly(ethylene glycol) in drug delivery: pros and cons as well as potential alternatives. *Angew. Chem. Int. Ed. Engl.* **49**, 6288–6308 (2010).
53. Qian, X. et al. Immunosuppressive effects of mesenchymal stem cells-derived exosomes. *Stem Cell Rev. Rep.* **17**, 411–427 (2021).
54. Kim, S. H. et al. Exosomes derived from IL-10-treated dendritic cells can suppress inflammation and collagen-induced arthritis. *J. Immunol.* **174**, 6440–6448 (2005).
55. Chaudhary, N., Weissman, D. & Whitehead, K. A. mRNA vaccines for infectious diseases: principles, delivery and clinical translation. *Nat. Rev. Drug Discov.* **20**, 817–838 (2021).
56. Peking, P., Koller, U. & Murauer, E. M. Functional therapies for cutaneous wound repair in epidermolysis bullosa. *Adv. Drug Deliv. Rev.* **129**, 330–343 (2018).
57. Vader, P., Mol, E. A., Pasterkamp, G. & Schiffelers, R. M. Extracellular vesicles for drug delivery. *Adv. Drug Deliv. Rev.* **106**, 148–156 (2016).
58. Born, L. J., Harmon, J. W. & Jay, S. M. Therapeutic potential of extracellular vesicle-associated long noncoding RNA. *Bioeng. Transl. Med.* **5**, e10172 (2020).
59. Pi, F. et al. Nanoparticle orientation to control RNA loading and ligand display on extracellular vesicles for cancer regression. *Nat. Nanotechnol.* **13**, 82–89 (2018).

Acknowledgements

We thank C. Wogan of the Division of Radiation Oncology, MD Anderson Cancer Center, for editorial assistance.

Author contributions

A.S.L. and F.L. conceived the work; A.S.L., W.J., F.L., Z.Y. and B.Y.S.K. supervised the research; A.S.L., J.S., L.J.L. and K.J.K. developed the technology; A.S.L., Y.Y., Y.T., F.L., W.J., Z.Y., L.T. and B.Y.S.K. designed the experiments; A.S.L., L.J.L., Z.Y., Y.T., Y.Y., W.J., F.L., B.Y.S.K., K.J.K., J.S., B.S., K.H., D.L., T.G., L.T., W.-J.L. and E.B. provided intellectual input; A.S.L., L.J.L., Z.Y., W.J., J.S., S.D., E.B. and B.Y.S.K. wrote the manuscript, with input from all authors; Y.Y., Y.T., J.S., K.J.K., Y.T., A.P.E., J.C., C.-L.C., W.-H.H. Y.L., Z.L., Y.Z., H.Z., X.L., Y.W. and J.H. conducted experiments; Y.Y., Y.T., Z.Y. and A.P.E. prepared figures and videos.

Competing interests

A.S.L. and L.J.L. are consultants and shareholders of Spot Biosystems, Ltd. J.S. and K.J.K are employees of Spot Biosystems, Ltd.

Additional information

Extended data is available for this paper at https://doi.org/10.1038/s41551-022-00989-w.

Supplementary information The online version contains supplementary material available at https://doi.org/10.1038/s41551-022-00989-w.

Correspondence and requests for materials should be addressed to Feng Lan, Betty Y. S. Kim or Andrew S. Lee.

Peer review information *Nature Biomedical Engineering* thanks Sun Hwa Kim, Chuanbin Wu and the other, anonymous, reviewer(s) for their contribution to the peer review of this work.

https://doi.org/10.1038/s41551-022-00989-w

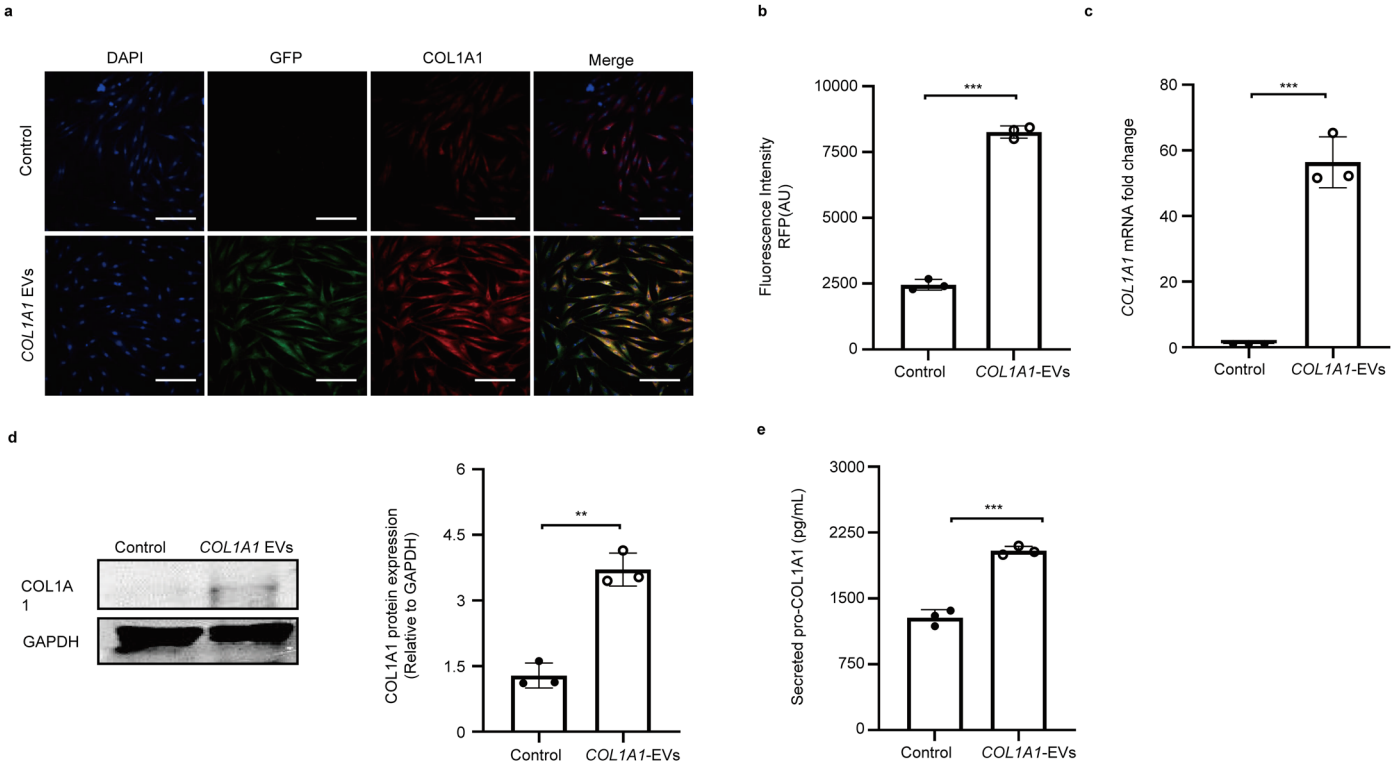

Extended Data Fig. 1 | *In vitro* delivery of COL1A1 mRNA-containing EVs. a, Fluorescence images of serum-starved nHDFs treated with *COL1A1-GFP* EVs and protein translated from delivered *COL1A1-GFP* mRNA after 48 h. Scale bar, 100 µm. **b**, Fluorescence intensity of cells treated with *COL1A1*-EVs (n = 3 for all groups, ***$P < 0.001$ Control vs *COL1A1*-EVs) in 48 h. **c**, RT-qPCR shows higher collagen mRNA transcript levels after *in vitro* delivery of *COL1A1* mRNA from EVs (n = 3 for all groups, ***$P < 0.001$ Control vs *COL1A1*-EVs) in 48 h. **d**, Western blots show elevated COL1A1 protein in treated fibroblasts (n = 3 for all groups, **$P = 0.001$ Control vs *COL1A1*-EVs).**e**, Pro-collagen I collected from supernatant and detected by ELISA (n = 3 for all groups, ***$P < 0.001$ Control vs *COL1A1*-EVs) in 48 h. All data are from three independent experiments and are presented as means ± SEM; two-sided Student's *t* tests were used for the comparisons in (**b**–**e**).

https://doi.org/10.1038/s41551-022-00989-w

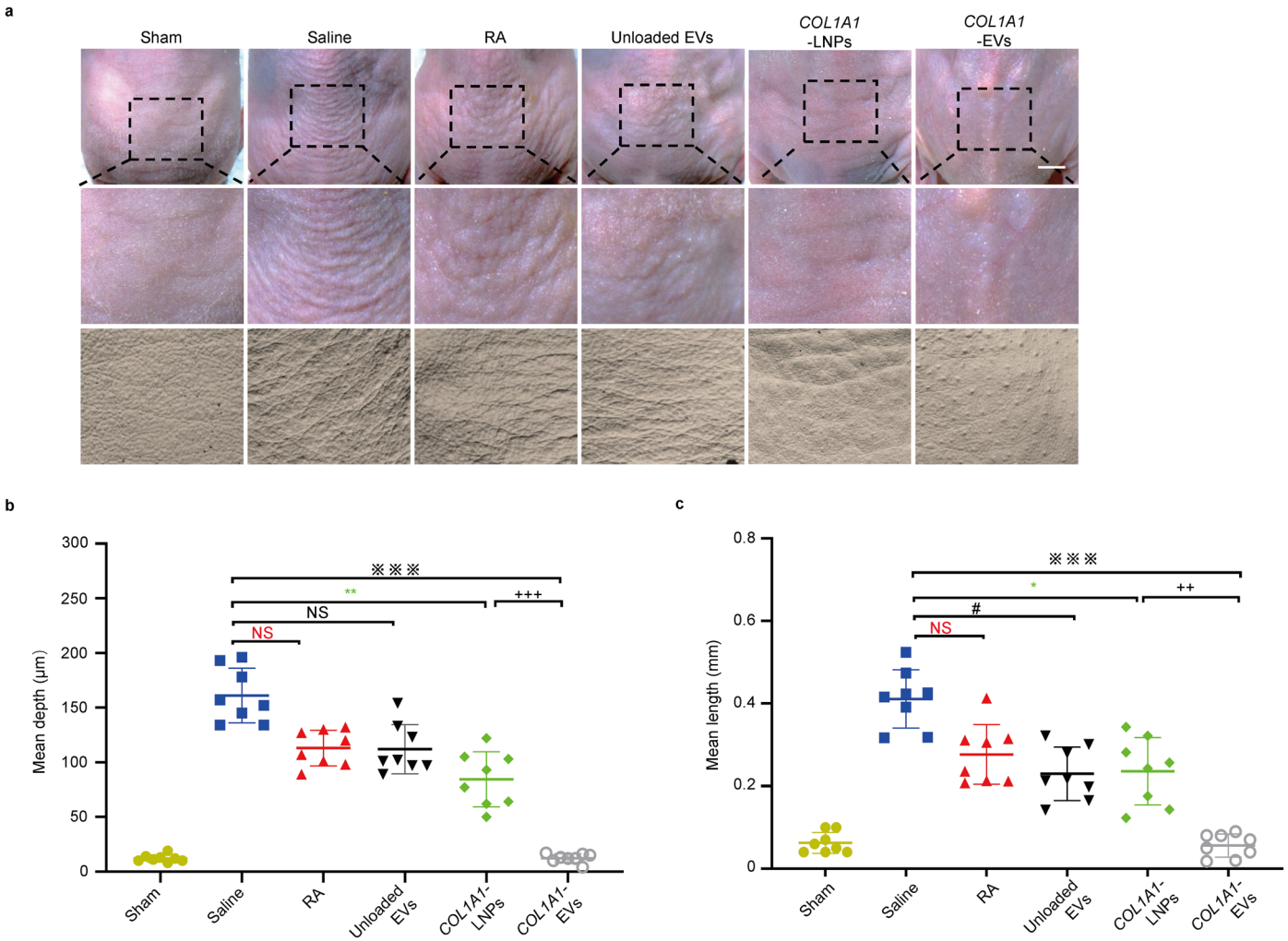

Extended Data Fig. 2 | Skin plaster assessment of dorsal skin after *COL1A1*-EV treatment. a, Microscopic observations of dorsal skin and skin replicas. Scale bar, 5 mm. **b**, Mean wrinkle depth in skin replicas (n = 4 for all groups, $^{***}P < 0.001$ *COL1A1*-EVs vs Saline; $^{**}P = 0.0025$ *COL1A1*-LNPs vs Saline; $^{+++}P < 0.001$ *COL1A1*-EVs vs *COL1A1*-LNPs). **c**, Mean wrinkle length analysed on skin replicas (n = 4 for all groups, $^{\#}P = 0.0203$ Unloaded EVs vs Saline; $^{*}P = 0.0405$ *COL1A1*-LNPs vs Saline; $^{***}P < 0.001$ *COL1A1*-EVs vs Saline; $^{++}P = 0.0015$ *COL1A1*-EVs vs *COL1A1*-LNPs). All data are from three independent experiments and are presented as means ± SEM. One-way analysis of variance (ANOVA) was used for the comparisons in (**b, c**). NS, not significant.

https://doi.org/10.1038/s41551-022-00989-w

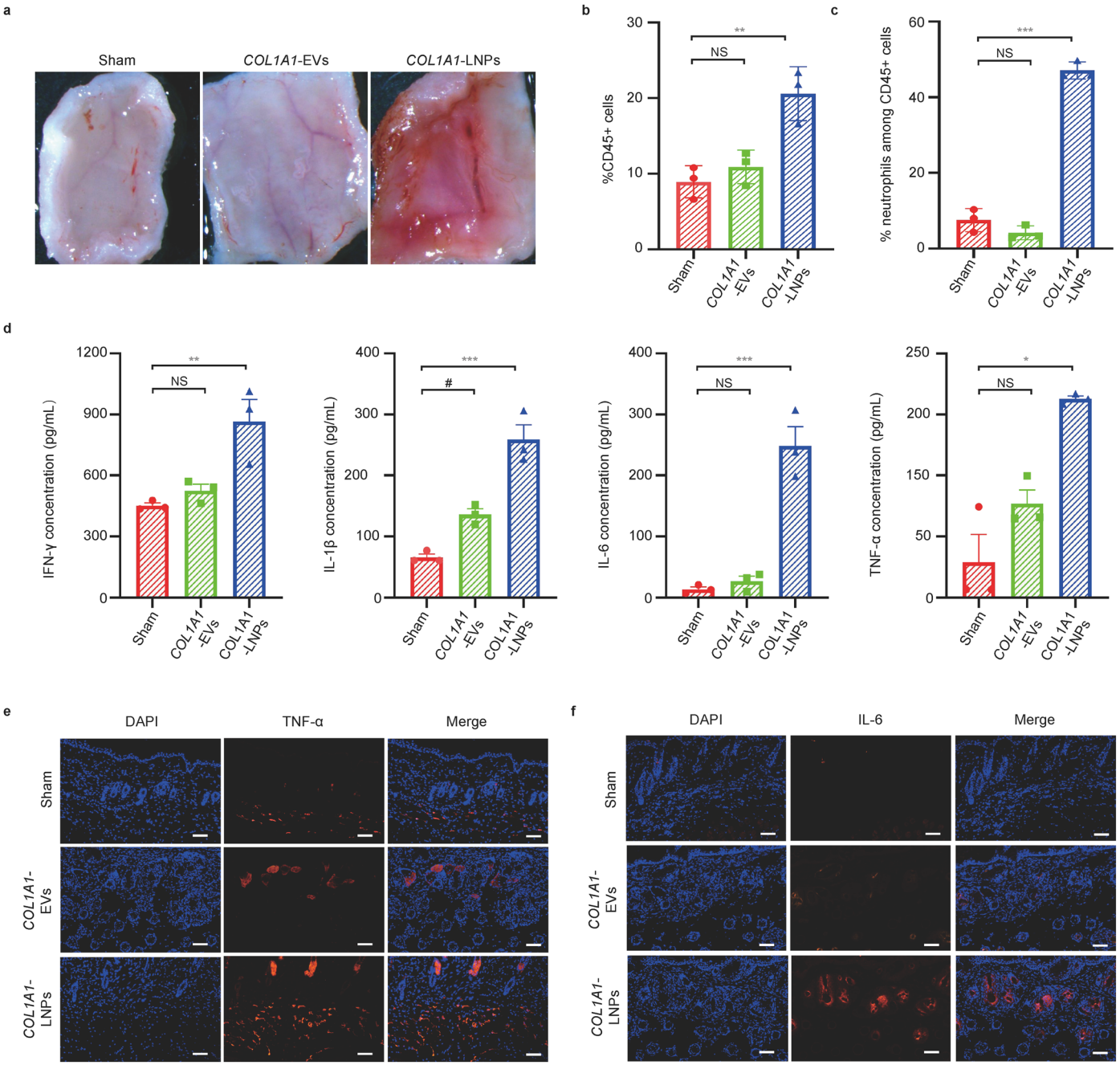

Extended Data Fig. 3 | Assessment of *in vivo* immunogenicity of *COL1A1*-LNPs and *COL1A1*-EVs. a, Skin samples from the mice injected with a single dose injection of 22E9 copy number *COL1A1* mRNA in *COL1A1*-EVs and *COL1A1*-LNPs were harvested after 24 h. Skin samples of mice were analysed by flow cytometry, for **b**, leukocyte cell percentage, and **c**, neutrophil percentage (n = 3 for all groups, $^{**}P = 0.0034$ *COL1A1*-LNPs vs sham for %CD45 + cells; $^{***}P < 0.001$ *COL1A1*-LNPs vs Sham for %neutrophils among CD45 + cells; NS, not significant). **d**, Protein quantification via ELISA for IFN-γ, IL-1β, IL-6 and TNF-α shows elevation of inflammatory cytokines in the *COL1A1*-LNPs group as compared to *COL1A1*-EVs (n = 3 for all groups, $^{**}P = 0.0074$ *COL1A1*-LNPs vs Sham for IFN-γ; $^{\#}P = 0.0333$ *COL1A1*-EVs vs Sham and $^{***}P < 0.001$ *COL1A1*-LNPs vs Sham for IL-1β; $^{***}P < 0.001$ *COL1A1*-LNPs vs Sham for IL-6; $^{*}P = 0.0146$ *COL1A1*-LNPs vs Sham for TNF-α; NS, not significant). **e**, Representative immunostaining images for TNF-α and (**f**) IL-6 after injected with *COL1A1*-EVs and *COL1A1*-LNPs. Scale bar, 100 μm. All data are from three independent experiments and are presented as means ± SEM. One-way ANOVA was used for the comparisons in (**b**–**d**).

https://doi.org/10.1038/s41551-022-00989-w

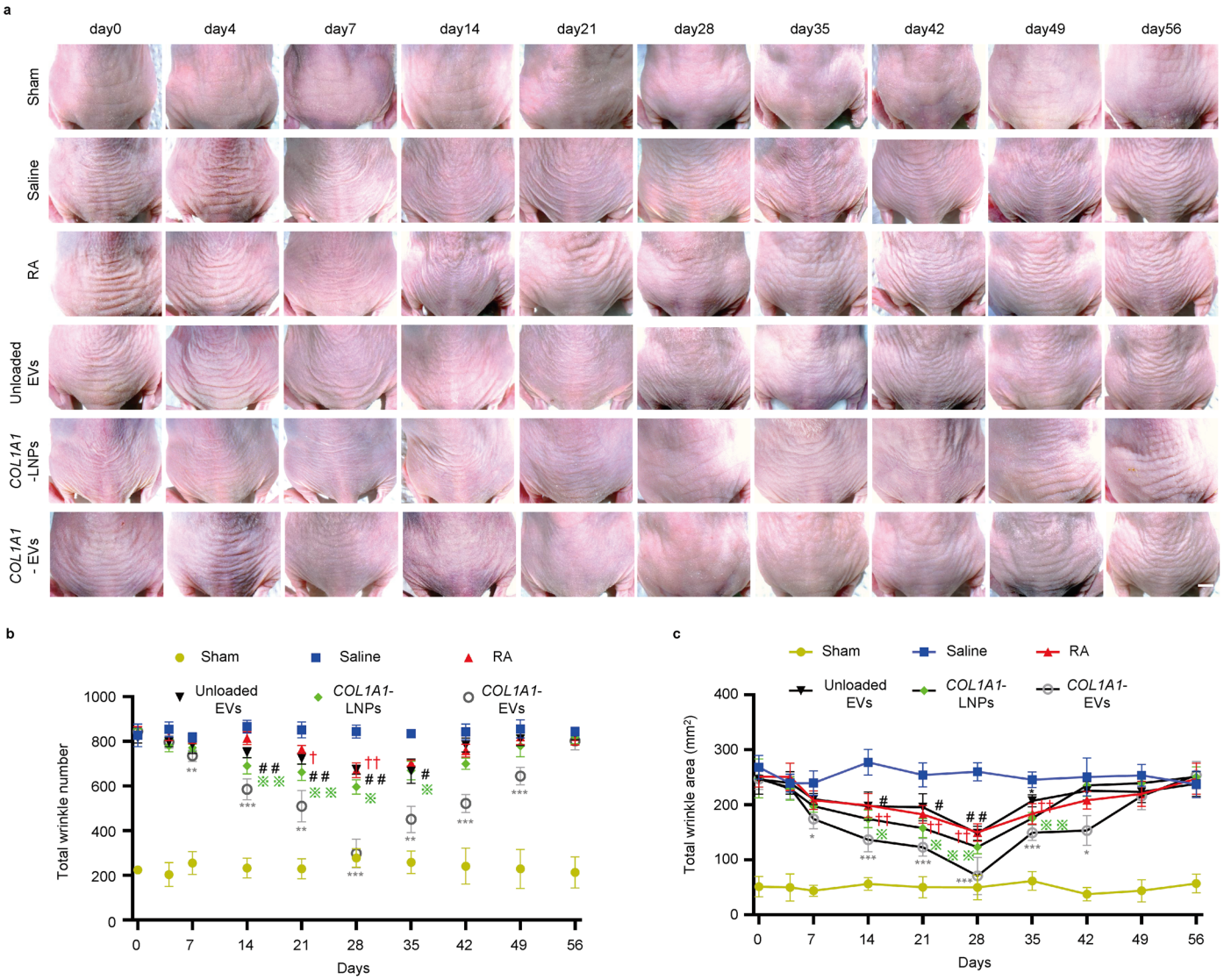

Extended Data Fig. 4 | Return of dermal wrinkles to baseline after treatment with low dose *COL1A1*-EVs. a, Wrinkles were tracked on days 0, 4, 7, 14, 21, 28, 35, 42, 49, and 56 d after the indicated treatments (5 low-dose injections of *COL1A1*-EVs (2.7E9 copy number *COL1A1* mRNA), *COL1A1*-LNPs (2.7E9 copy number *COL1A1* mRNA), unloaded EVs, 0.05% retinoic acid [RA], saline). n = 4, Scale bar, 5 mm. Female nude mice that were not exposed to UV comprised the sham group. **b**, Numbers of wrinkles on the dorsal skin of the mice over time. (n = 4 for all groups; $^{**}P = 0.008$ *COL1A1*-EVs vs Saline at day 7; $^{**}P = 0.004$ *COL1A1*-EVs vs Saline at day 21, $^{**}P = 0.001$ *COL1A1*-EVs vs Saline at day 35; $^{***}P < 0.001$ *COL1A1*-EVs vs Saline at days 14, 28, 42, and 49; $^{\dagger}P = 0.025$ RA vs Saline at day 21; $^{\dagger\dagger}P = 0.007$ RA vs Saline at day 28; $^{\#\#}P = 0.0071$ Unloaded EVs vs Saline at day 14; $^{\#\#}P = 0.004$ Unloaded EVs vs Saline at day 21; $^{\#\#}P = 0.002$ Unloaded EVs vs Saline at day 28; $^{\#}P = 0.015$ Unloaded EVs vs Saline at day 35; $^{※※}P = 0.0053$ *COL1A1*-LNPs vs Saline at day 14; $^{※※}P = 0.0041$ *COL1A1*-LNPs vs Saline at day 21; $^{※}P = 0.017$ *COL1A1*-LNPs vs Saline at day 28; $^{※}P = 0.022$ *COL1A1*-LNPs vs Saline at day 35). **c**, Total wrinkle area (n = 4 for all groups, $^{*}P = 0.012$ *COL1A1*-EVs vs Saline at day 7; $^{***}P < 0.001$ *COL1A1*-EVs vs Saline at days 14, 21, 28 and 35; $^{*}P = 0.015$ *COL1A1*-EVs vs Saline at day 42; $^{\dagger\dagger}P = 0.008$ RA vs Saline at day 14; $^{\dagger\dagger}P = 0.007$ RA vs Saline at days 21 and 35; $^{\dagger\dagger}P = 0.005$ RA vs Saline at day 28; $^{\#}P = 0.012$ Unloaded EVs vs Saline at day 14; $^{\#}P = 0.035$ Unloaded EVs vs Saline at day 21; $^{\#\#}P = 0.002$ Unloaded EVs vs Saline at day 28; $^{※}P = 0.062$ *COL1A1*-LNPs vs Saline at day 14; $^{※}P = 0.039$ *COL1A1*-LNPs vs Saline at day 21; $^{※※}P = 0.0027$ *COL1A1*-LNPs vs Saline at day 28; $^{※※}P = 0.046$ *COL1A1*-LNPs vs Saline at day 35). All data are from three independent experiments and are presented as means ± SEM. Two-way ANOVA was used for the comparisons in (**b, c**).

https://doi.org/10.1038/s41551-022-00989-w

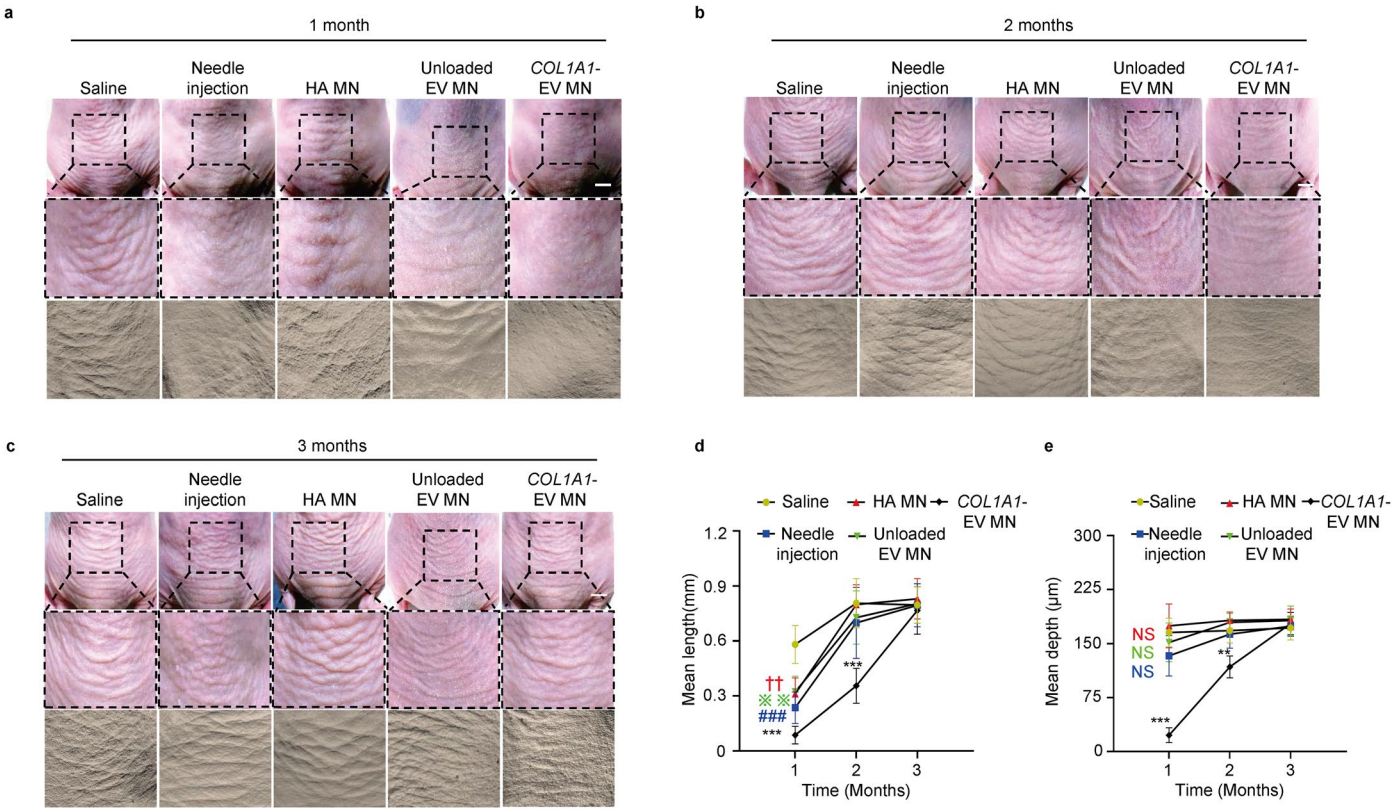

Extended Data Fig. 5 | Evaluation of long term *COL1A1*-EV MN dermal wrinkle treatment by skin replica plaster. a–c, Microscopic observation of dorsal skin and skin replica at 1 month, 2 months, and 3 months after treatment. Scale bar, 5 mm. **d, e** Quantification of mean wrinkle length (n = 4 for all groups, ***$P < 0.001$ *COL1A1*-EV MN vs Saline at 1 month and 2 months; $^{###}P < 0.001$ Needle injection vs Saline at 1 month; $^{††}P = 0.031$ HA MN vs Saline at 1 month; $^{※※}P = 0.029$ Unloaded EV MN vs Saline at 1 month) and mean wrinkle depth (n = 4 for all groups, ***$P < 0.001$ *COL1A1*-EV MN vs Saline at 1 month; **$P = 0.001$ *COL1A1-EV MN* vs Saline at 2 months; Needle injection vs Saline not significant at 1 month; HA MN vs Saline not significant at 1 month) from skin replicas. All data are from three independent experiments and are presented as means ± SEM. Two-way ANOVA was used for the comparisons in (**d, e**).

https://doi.org/10.1038/s41551-022-00989-w

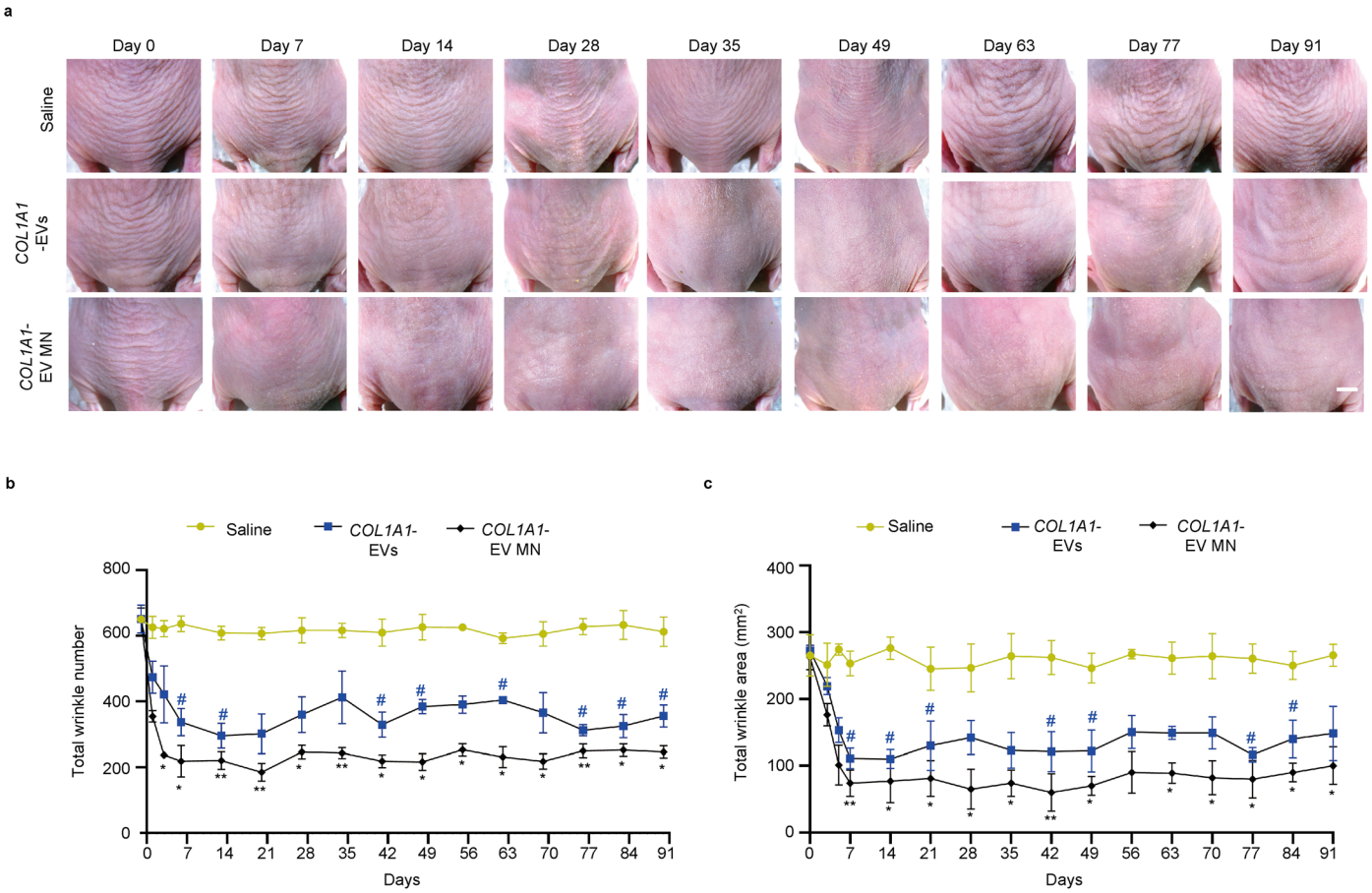

Extended Data Fig. 6 | Maintenance of wrinkle treatment via serial injection of *COL1A1*-EVs and *COL1A1*-EV MN. a, After 8 weeks of UV irradiated photoaging, wrinkles were tracked for mice treated every 30 days with 1) saline, 2) *COL1A1*-EVs, and 3) *COL1A1*-EV MN on days 0, 4, 7, 14, 21, 28, 49, 70, and 91 (*COL1A1*-EVs, *COL1A1*-EV MN, Saline). n = 4, Scale bar, 5 mm. **b**, Total wrinkle number (n = 4 for all groups; $^{*}P = 0.019$ *COL1A1*-EV MN vs Saline at day 4; $^{\#}P = 0.034$ *COL1A1*-EVs vs Saline, $^{*}P = 0.031$ *COL1A1*-EV MN vs Saline at day 7; $^{\#}P = 0.030$ *COL1A1*-EVs vs Saline, $^{**}P = 0.008$ *COL1A1*-EV MN vs Saline at day 14; $^{**}P = 0.008$ *COL1A1*-EV MN vs Saline at day 21; $^{*}P = 0.025$ *COL1A1*-EV MN vs Saline at day 28; $^{**}P = 0.006$ *COL1A1*-EV MN vs Saline at day 35; $^{\#}P = 0.031$ *COL1A1*-EVs vs Saline, $^{*}P = 0.030$ *COL1A1*-EV MN vs Saline at day 42; $^{\#}P = 0.044$ *COL1A1*-EVs vs Saline, $^{*}P = 0.016$ *COL1A1*-EV MN vs Saline at day 49; $^{*}P = 0.016$ *COL1A1*-EV MN vs Saline at day 56; $^{\#}P = 0.017$ *COL1A1*-EVs vs Saline, $^{*}P = 0.020$ *COL1A1*-EV MN vs Saline at day 63; $^{*}P = 0.018$ *COL1A1*-EV MN vs Saline at day 70; $^{\#}P = 0.011$ *COL1A1*-EVs vs Saline, $^{**}P = 0.006$ *COL1A1*-EV MN vs Saline at day 77; $^{\#}P = 0.028$ *COL1A1*-EVs vs Saline, $^{*}P = 0.037$ *COL1A1*-EV MN vs Saline at day 84; $^{\#}P = 0.043$ *COL1A1*-EVs vs Saline, $^{*}P = 0.043$ *COL1A1*-EV MN vs Saline at day 91) and **c**, wrinkle area on the dorsal skin of the mice during 90 day study window (n = 4 for all groups; $^{\#}P = 0.012$ *COL1A1*-EVs vs Saline, $^{**}P = 0.005$ *COL1A1*-EV MN vs Saline at day7; $^{\#}P = 0.010$ *COL1A1*-EVs vs Saline, $^{*}P = 0.048$ *COL1A1*-EV MN vs Saline at day 14; $^{\#}P = 0.023$ *COL1A1*-EVs vs Saline, $^{*}P = 0.021$ *COL1A1*-EV MN vs Saline at day 21; $^{*}P = 0.022$ *COL1A1*-EV MN vs Saline at day 28; $^{*}P = 0.046$ *COL1A1*-EV MN vs Saline at day 35; $^{\#}P = 0.019$ *COL1A1*-EVs vs Saline, $^{**}P = 0.009$ *COL1A1*-EV MN vs Saline at day 42; $^{\#}P = 0.042$ *COL1A1*-EVs vs Saline, $^{*}P = 0.030$ *COL1A1*-EV MN vs Saline at day 49; $^{*}P = 0.030$ *COL1A1*-EV MN vs Saline at day63; $^{*}P = 0.029$ *COL1A1*-EV MN vs Saline at day 70; $^{\#}P = 0.048$ *COL1A1*-EVs vs Saline, $^{*}P = 0.022$ *COL1A1*-EV MN vs Saline at day 77; $^{\#}P = 0.040$ *COL1A1*-EVs vs Saline, $^{*}P = 0.027$ *COL1A1*-EV MN vs Saline at day 84; $^{*}P = 0.045$ *COL1A1*-EV MN vs Saline at day 91). All data are from three independent experiments and are presented as means ± SEM. Two-way ANOVA was used for the comparisons in (**b, c**).

nature portfolio

Corresponding author(s): Feng Lan, Betty Y.S . Kim and Andrew S. Lee

Last updated by author(s): Aug 4, 2022

Reporting Summary

Nature Portfolio wishes to improve the reproducibility of the work that we publish. This form provides structure for consistency and transparency in reporting. For further information on Nature Portfolio policies, see our Editorial Policies and the Editorial Policy Checklist.

Statistics

For all statistical analyses, confirm that the following items are present in the figure legend, table legend, main text, or Methods section.

n/a	Confirmed
☐	☒ The exact sample size (*n*) for each experimental group/condition, given as a discrete number and unit of measurement
☐	☒ A statement on whether measurements were taken from distinct samples or whether the same sample was measured repeatedly
☐	☒ The statistical test(s) used AND whether they are one- or two-sided *Only common tests should be described solely by name; describe more complex techniques in the Methods section.*
☒	☐ A description of all covariates tested
☐	☒ A description of any assumptions or corrections, such as tests of normality and adjustment for multiple comparisons
☐	☒ A full description of the statistical parameters including central tendency (e.g. means) or other basic estimates (e.g. regression coefficient) AND variation (e.g. standard deviation) or associated estimates of uncertainty (e.g. confidence intervals)
☐	☒ For null hypothesis testing, the test statistic (e.g. *F*, *t*, *r*) with confidence intervals, effect sizes, degrees of freedom and *P* value noted *Give P values as exact values whenever suitable.*
☒	☐ For Bayesian analysis, information on the choice of priors and Markov chain Monte Carlo settings
☒	☐ For hierarchical and complex designs, identification of the appropriate level for tests and full reporting of outcomes
☒	☐ Estimates of effect sizes (e.g. Cohen's *d*, Pearson's *r*), indicating how they were calculated

Our web collection on statistics for biologists contains articles on many of the points above.

Software and code

Policy information about availability of computer code

Data collection	ImageJ 1.53a
Data analysis	ImageJ 1.53a, GraphPad Prism 8.3

For manuscripts utilizing custom algorithms or software that are central to the research but not yet described in published literature, software must be made available to editors and reviewers. We strongly encourage code deposition in a community repository (e.g. GitHub). See the Nature Portfolio guidelines for submitting code & software for further information.

Data

Policy information about availability of data

All manuscripts must include a data availability statement. This statement should provide the following information, where applicable:

- Accession codes, unique identifiers, or web links for publicly available datasets
- A description of any restrictions on data availability
- For clinical datasets or third party data, please ensure that the statement adheres to our policy

The main data supporting the results in this study are available within the paper and its Supplementary Information. Source data for the figures are available from figshare at https://figshare.com/articles/dataset/SD_FIGS_xlsx/21514641. The raw and analysed datasets generated during the study are available for research purposes from the corresponding authors on reasonable request.

Human research participants

Policy information about studies involving human research participants and Sex and Gender in Research.

Reporting on sex and gender	The study did not involve human research participants.
Population characteristics	—
Recruitment	—
Ethics oversight	—

Note that full information on the approval of the study protocol must also be provided in the manuscript.

Field-specific reporting

Please select the one below that is the best fit for your research. If you are not sure, read the appropriate sections before making your selection.

☒ Life sciences ☐ Behavioural & social sciences ☐ Ecological, evolutionary & environmental sciences

For a reference copy of the document with all sections, see nature.com/documents/nr-reporting-summary-flat.pdf

Life sciences study design

All studies must disclose on these points even when the disclosure is negative.

Sample size	Sample sizes were determined on the basis of previous experimental experience (Nat Biomed Eng. 4, 69–83 (2020); Nat Biomed Eng. 2, 104–113 (2018)). For the in vitro study, all experiments were performed with at least 3 independent samples. According to another study (ACS Nano. 2019;13(10):11273-11282), our in vivo sample size was sufficient to perform statistical analyses.
Data exclusions	No data were excluded.
Replication	All attempts at replication were successful.
Randomization	All samples and animals were randomly assigned to each group.
Blinding	Data collection and data analysis were blinded.

Reporting for specific materials, systems and methods

We require information from authors about some types of materials, experimental systems and methods used in many studies. Here, indicate whether each material, system or method listed is relevant to your study. If you are not sure if a list item applies to your research, read the appropriate section before selecting a response.

Materials & experimental systems

n/a	Involved in the study
☐	☒ Antibodies
☐	☒ Eukaryotic cell lines
☒	☐ Palaeontology and archaeology
☐	☒ Animals and other organisms
☒	☐ Clinical data
☒	☐ Dual use research of concern

Methods

n/a	Involved in the study
☒	☐ ChIP-seq
☐	☒ Flow cytometry
☒	☐ MRI-based neuroimaging

Antibodies

Antibodies used	The following antibodies were used: anti-CD63 antibody from Abcam, Catalog number:ab68418, Clonality: Polyclonal anti-GAPDH antibody from Abcam, Catalog number:ab8245, Clonality: monoclonal anti-CD9 antibody from cell signaling, Catalog number:13403S, Clonality: monoclonal anti-Tsg101 antibody from Abcam, Catalog number:ab125011, Clonality: Monoclonal anti-Arf antibody from Abcam, Catalog number:ab77581, Clonality: Polyclonal

anti-Collagen I antibody from Abcam, Catalog number:ab34710, Clonality: Polyclonal
anti-GFP antibody from Abcam,Catalog number:ab6556, Clonality:Polyclonal
anti-MMP1 antibody from Abcam,Catalog number:ab137332, Clonality:Polyclonal
anti-Elastin antibody from Bioss,Catalog number:bs-11057R, Clonality:Polyclonal
anti-TNF alpha antibody from Abcam,Catalog number:ab183218, Clonality:Monoclonal
anti-TGF beta 1 antibody from Abcam,Catalog number:ab215715, Clonality:Monoclonal
anti-IL-1 beta antibody from Abcam,Catalog number:ab234437, Clonality:Monoclonal

Validation

The antibodies were validated by the manufacturers.

Eukaryotic cell lines

Policy information about cell lines and Sex and Gender in Research

Cell line source(s)	The cell lines were purchased from ATCC.
Authentication	The cell lines were authenticated by the supplier by using mycoplasma analysis.
Mycoplasma contamination	The cells line were tested by PCR and were negative for mycoplasma.
Commonly misidentified lines (See ICLAC register)	No commonly misidentified cell lines were used.

Animals and other research organisms

Policy information about studies involving animals; ARRIVE guidelines recommended for reporting animal research, and Sex and Gender in Research

Laboratory animals	BALB/C-nu, 10–12 weeks old, were used.
Wild animals	The study did not involve wild animals.
Reporting on sex	Female nude mice were used for skin-photoaging modelling.
Field-collected samples	The study did not involve samples collected from the field.
Ethics oversight	The animal experiments were approved by Animal Ethics Committee of the Shenzhen Bay Laboratory (No.D2021-107) and by CRO. All experimental procedures were conducted in accordance with laboratory animal guidelines.

Note that full information on the approval of the study protocol must also be provided in the manuscript.

Flow Cytometry

Plots

Confirm that:

☒ The axis labels state the marker and fluorochrome used (e.g. CD4-FITC).

☒ The axis scales are clearly visible. Include numbers along axes only for bottom left plot of group (a 'group' is an analysis of identical markers).

☒ All plots are contour plots with outliers or pseudocolor plots.

☒ A numerical value for number of cells or percentage (with statistics) is provided.

Methodology

Sample preparation	The mice were sacrificed and 1 cm2 sof kin tissue was harvested from the injected area. To prepare cells for flow-cytometry analysis, collagenase (Sigma, cat#C7657), hyaluronidase (Sigma, cat#H3884) were used, as described in Supplementary methods. Pre-warmed 9-mL cell medium was used to separate the single cells from tissues.
Instrument	ACEA NovoCyte
Software	FLowJo Version 10 was used for analysis.
Cell population abundance	Supplementary Figs. 7b,c show the percentages of certain cell populations.
Gating strategy	The major cells were initially on a dot plot, SSC-A vs. FSC-A. The negative population was determined by unstained cell control.

☒ Tick this box to confirm that a figure exemplifying the gating strategy is provided in the Supplementary Information.